Ocean Mixed Layer Mean Kinetic Energy and Vorticity Budgets Forced by Mature Tropical Cyclones

Dissertation Proposal for
Ph.D. in Meteorology and Physical Oceanography

Eric W. Uhlhorn

Division of Meteorology and Physical Oceanography
Rosenstiel School of Marine and Atmospheric Science
University of Miami

June 19, 2005

1. Introduction

Tropical cyclones are among the most intense organized vortical systems observed in the atmosphere. These cyclones derive their energy primarily from the release of latent heat upon condensation of water vapor (Ooyama 1969). Thus, it is necessary that a large moisture source be present, such as the ocean, and that the ocean surface temperature is sufficiently warm to maintain a moisture flux from the sea to the atmospheric boundary layer, as was first recognized by Palmen (1948). Numerous other studies have examined the relationship between the intensity of tropical cyclones (TCs) and the sea surface temperature (SST). Malkus and Riehl (1960) derived a relationship between the decrease in central pressure and the increase in equivalent potential temperature in the eyewall region (due to imported enthalpy from the ocean). Further studies by Emanuel (1986) and Betts and Simpson (1987) confirmed this relationship to be approximately constant. More recent research has studied not only the influence of SST on TC intensity but the relationship between intensity and the upper ocean thermal energy (Shay et al. 2000).

Because the underlying ocean significantly modulates TC intensity, much attention has been drawn toward gaining a better understanding of the physical interaction between the atmosphere and ocean during these events. Unfortunately, due to limited observational data at the air-sea interface in high-wind conditions, the understanding has not progressed nearly enough to significantly improve the parameterization of momentum and energy transfer. The relationships of the transfer processes to small-scale roughness (Charnock relation) and surface-layer stability (Monin-Obukhov similarity theory) are fairly well understood under low-wind conditions (e.g. Large and Pond (1981)), but additional phenomena not typically observed such as the maturity of the sea state (Donelan et al. 1993) and spray (Fairall et al. 1994) have also been shown to modulate the heat and momentum exchange. These effects have been studied in the field at sub hurricane-force conditions (Katsaros et al. 1987; Donelan et al. 1997), and at high winds in controlled laboratory experiments (Alamaro et al. 2002; Donelan et al. 2004), but to date have not been verified

in actual storms. The Office of Naval Research sponsored Coupled Boundary Layer Air-Sea Transfer (CBLAST) field experiment in 2003-2004 was designed to address these issues; results are pending.

A TC's intensity is maintained in part by the balance between the heat gained by the boundary layer of the storm and the energy lost due to friction. Emanuel (1986) proposed an air-sea interaction theory requiring this relative balance to be the *primary* modulator of intensity. Based on this view, it seems reasonable to assume that under certain conditions there should be a level of mutual dependence of the air-sea transfer processes of heat and momentum. Indeed, it has been suggested through highly idealized model simulations (Ooyama 1969; Rosenthal 1971; Emanuel 1995; Braun and Tao 2000) that a TC's intensity is sensitive to the ratio of enthalpy transfer coefficient to drag coefficient (C_k/C_d). Additionally, the conclusion that this quantity probably lies within a rather limited range (≤ 1.5) is commensurate with the observation that most TCs do not typically reach their maximum potential intensity (DeMaria and Kaplan 1993).

One rationale is that if not all wind energy dissipates at the air/sea interface, an increase of kinetic energy (KE) in the upper ocean should be realized. Observations of wind profiles in hurricanes within the atmospheric surface layer do generally show logarithmic behavior (Powell et al. 2003), indicative of the significant shear that is present. But the sea surface deforms under stress and absorbs a portion of the KE of the wind, and thus not all wind energy dissipates into internal energy of the atmospheric boundary layer. The ocean roughens in response to pressure perturbations associated with Reynolds stress in the form of gravity-capillary waves. Continued wind stress will cause wave energy growth; when these waves have reached a point of gravitational instability they will break (Huang 1986). Some of the lost wave energy is transferred to the KE of the ocean mixed layer (OML), and the mean flow (current) accelerates. Both the local wave energy and wind stress must therefore be determined to ascertain the rate of KE transfer from the wind to the currents.

The wind stress (or momentum flux) at the air-sea interface is typically parameterized in terms of the mean wind speed just above the sea surface through a wind speed-dependent drag coefficient (C_d). Numerous C_d formulations have been suggested, and nearly all published results are based on observations in winds speeds $< 25\ \mathrm{m\,s^{-1}}$ (e.g. Garratt (1977); Large and Pond (1981)). Results generally show a linear increase in C_d with wind speed above $5\ \mathrm{m\,s^{-1}}$ through the applicable range, but beyond the upper limit there is considerable uncertainty. If, in fact, the drag continues to increase indefinitely, some other physical process must be important at high winds to maintain the surface energy balance. Evaporation of sea spray droplets has been proposed as a possible mechanism responsible for the significant enthalpy flux in TC winds necessary to balance this increased drag (Andreas and Emanuel 2001). Other studies representing a counter argument have suggested a possible decrease in the slope of the wind speed dependence near hurricane force (Alamaro et al. 2002; Powell et al. 2003; Donelan et al. 2004; Shay and Jacob 2005). Based on field observations, Shay and Jacob (2005) report this transition occurring at 28-30 $\mathrm{m\,s^{-1}}$, and recent laboratory experiments by Donelan et al. (2004) suggest this slope change occurring at around 33 $\mathrm{m\,s^{-1}}$. A recently proposed hypothesis about the physical nature suggests that at extreme wind speeds, a spray filled transition zone develops at the air-sea interface, such that the exchange processes scale only with fluid properties of this zone, implying a wind-speed independence and self similarity (Emanuel 2003). To date, none of these hypotheses have been directly verified in the field, and with this uncertainty comes the lack of knowledge of just how much momentum and KE is actually lost by a tropical cyclone to the upper ocean.

The early observational study of Leipper (1967) has motivated extensive research of the OML response to hurricane forcing. Most previous studies have focused on the upper ocean thermal energy response (Price 1981; Black 1983; Brooks 1983). Numerical studies (O'Brien and Reid 1967; Chang and Anthes 1978; Price 1983) have provided additional insight into the coupling between the mechanical and thermal

energy response, but in general the role of the storm-generated current field on the ocean temperature change could only be verified through comparison with linear solutions (Geisler 1970). Since the entrainment process is believed to be the dominant OML cooling mechanism over surface heat flux (Price 1981), the lack of momentum data prevented a quantitative budgetary closure in most early work.

Shay and Elsberry (1987) were able to examine the OML and thermocline current response to Hurricane Frederic (1979) with sufficient resolution to quantify both the vertical flux of energy through the OML as well as the internal wave wake response that is predicted by linear theory. Using a series of expendable current probes (AXCP) deployed in Hurricane Gilbert (1988), Shay et al. (1998) isolated the geostrophic and near-inertial current in the vertical structure. With these data, Jacob et al. (2000) studied the effect of the pre-existing current field on the advective tendency of OML cooling. In conjunction with this observational effort, Jacob et al. (2000) conducted a series of numerical experiments to examine differences in the simulated ocean response based on the choice of vertical mixing parameterization. In virtually all previous studies of OML response, the surface stress was assumed known and often unquestioned.

In his numerical simulation of the ocean's internal wave wake response to a TC-like storm, Price (1983) used energy and vorticity conservation relations to diagnose model results. In the research proposed herein, similar diagnostic methods are applied to upper-ocean observations of kinematic and thermodynamic structure within the directly-forced region below a hurricane. This particular study, on the other hand, differs significantly from previous research, in that the source terms in the budget equations are not assumed known, but are instead estimated as residuals required to close the budgets. These estimates are then examined relative to assumed stress computed from the observed surface wind combined with documnented stress parameterizations. Finally, an evaluation of simulated fields by the GFDL operational coupled atmosphere-ocean hurricane model system will be made based on estimates of these observed and derived quantities.

2. Goal and objectives

The primary goal of this research is: *To quantify the observed mean kinetic energy and vorticity budgets of the ocean mixed layer forced by a tropical cyclone.* In support of the primary goal, the scientific objectives of this proposed research are:

- Compute the mechanical energy and vorticity budget equations' terms derived primarily from observed vertical profiles of horizontal currents and thermodyanmic variables;
- Compare the surface energy flux and wind stress curl (estimated as budget residuals) to that associated with the observed surface wind forcing combined with documented wind stress parameterizations, and;
- Evaluate the National Weather Service's operational GFDL coupled atmosphere-ocean model predictions based on the observed quantities.

To address the research objectives, a combined observational and numerical study focusing on Hurricane Lili (2002) is proposed. As part of the NOAA/Hurricane Research Division's (HRD) field program, a joint NSF/NOAA experiment was designed to measure the evolution of the upper ocean response to a hurricane. The objectives of the experiment were to be met through a series of research aircraft flights by deploying expendable ocean and atmospheric data probes prior to, during, and after passage of the storm. Hurricane Lili provided an ideal situation in order to meet these objectives. By combining the efforts of three NOAA aircraft, the cyclone and its environment was sampled nearly continuously as it traversed the Gulf of Mexico from western Cuba on its way to landfall in Louisiana. A dense grid of upper-ocean thermal data was measured by AXBT, AXCTD and AXCP, and the current field was sampled using AXCP. In addition, the long-wave portion of the surface wave directional spectrum was measured within the storm by the NASA Scanning Radar Altimeter (SRA) (Wright et al. 2001). Finally, a high-resolution wind field

was observed directly at the surface by the HRD Stepped Frequency Microwave Radiometer (SFMR) (Uhlhorn and Black 2003).

3. Background

a. Mechanical energy equation

The governing equation of motion for a fluid flow is Newton's 2nd Law. Following Kundu (1990), the equation of motion is:

$$\rho \frac{Du_i}{Dt} = \rho g_i + \frac{\partial \tau_{ij}}{\partial x_j}, \tag{1}$$

which states that, following the motion of a fluid parcel of unit volume, the rate of change of momentum $\rho Du_i/Dt$ is the net result of a field (body) force ρg_i and a surface force $\partial \tau_{ij}/\partial x_j$. Expressed in a coordinate system rotating at an angular velocity Ω_j, the equation of motion is:

$$\rho \frac{Du_i}{Dt} = \rho g_i + \frac{\partial \tau_{ij}}{\partial x_j} - 2\rho \epsilon_{ijk} \Omega_j u_k, \tag{2}$$

where ϵ_{ijk} is the alternating unit tensor defined as +1 for cyclic indicial permutations, -1 for anti-cyclic permutations, and 0 for any two or more equal idicies. This additional term represents the Coriolis acceleration.

An equation for the rate of change of kinetic energy (KE) is obtained by multiplying Equation 2 by u_i (i.e. scalar multiplication) and summing over i:

$$\rho \frac{Dk}{Dt} = \rho u_i g_i + u_i \frac{\partial \tau_{ij}}{\partial x_j}. \tag{3}$$

Equation 3 is the simplest form of the *mechanical energy equation*, which states that an increase in KE per unit mass $k = (u_i u_i)/2$ is the net result of the work done by a body force $\rho u_i g_i$ and a surface force $u_i \partial \tau_{ij}/\partial x_j$. The Coriolis acceleration does no work and is contracted from the problem since the alternat-

ing unit tensor prevents u_i from equaling u_k (i.e. the Coriolis acceleration acts normal to the flow).

The divergence of the stress tensor times the velocity is seen to increase the KE of a fluid element. But because the total work done on a fluid element is $\partial(u_i\tau_{ij})/\partial x_j$, a remaining part goes into deforming the element, and increasing its internal energy. This can be seen by performing product differentiation on the total work:

$$\underbrace{\frac{\partial(u_i\tau_{ij})}{\partial x_j}}_{\text{Total work}} = \underbrace{\tau_{ij}\frac{\partial u_i}{\partial x_j}}_{\text{Deformation}} + \underbrace{u_i\frac{\partial \tau_{ij}}{\partial x_j}}_{\text{Increase in KE}} \quad . \tag{4}$$

Since the deformation work contains a doubly-contracted product of the symmetric stress tensor $\tau_{ij} = \tau_{ji}$ with the tensor $\partial u_i/\partial x_j$, the deformation term may be written as the product of the stress tensor with the symmetric part of $\partial u_i/\partial x_j = e_{ij}$:

$$\tau_{ij}\frac{\partial u_i}{\partial x_j} = \tau_{ij}e_{ij}, \tag{5}$$

where:

$$e_{ij} = \frac{1}{2}\left(\frac{\partial u_i}{\partial x_j} + \frac{\partial u_j}{\partial x_i}\right) \tag{6}$$

is the strain rate tensor. Assuming a Newtonian fluid, the stress can be related to the fluid properties using the constitutive equation assuming approximate incompressibility:

$$\tau_{ij} = -p\delta_{ij} + 2\mu e_{ij}, \tag{7}$$

with $p = \tau_{jj}$ the normal (diagonal) components of the stress tensor. Upon multiplication of the constitutive

equation with the strain rate tensor, the deformation work becomes:

$$\underbrace{\tau_{ij}\frac{\partial u_i}{\partial x_j}}_{\text{Deformation}} = \underbrace{-p\frac{\partial u_j}{\partial x_j}}_{\text{Compression}} + \underbrace{2\mu e_{ij}e_{ij}}_{\text{Dissipation}}, \tag{8}$$

which has made use of the relation $e_{ij}\delta_{ij} = e_{jj} = \partial u_j/\partial x_j$. The deformation work consists of a reversible component due to compressibility effects, and an irreversible component due to continuous viscous drain.

Upon substitution of Equation 8, along with the definition of total work done by surface forces (Equation 4), the mechanical energy equation can now be written as:

$$\rho\frac{Dk}{Dt} = \underbrace{\rho u_i g_i}_{1} + \underbrace{\frac{\partial(u_i\tau_{ij})}{\partial x_j}}_{2} + \underbrace{p\left(\frac{\partial u_j}{\partial x_j}\right)}_{3} - \underbrace{2\mu\left(\frac{\partial u_i}{\partial x_j}\right)^2}_{4}, \tag{9}$$

which now states that following the motion, the rate of KE density change results from:

1. Work done on the volume by the body force;
2. Energy flux across volume surfaces due to the normal components of the stress tensor;
3. KE exchanges with internal energy (heat) by volume expansion; and,
4. KE loss within the volume through viscous dissipation, which irreversibly converts KE into internal energy.

b. Vorticity equation

The equation for the rate of change of relative vorticity is derived from the equations of motion in a rotating coordinate system (Equation 2). By substituting the Newtonian constitutive equation for an

incompressible fluid (Equation 7), the Navier-Stokes momentum equations are:

$$\frac{Du_i}{Dt} = -\frac{1}{\rho}\frac{\partial p}{\partial x_i} + g_i + \frac{1}{\rho}\frac{\partial \tau_{ij}}{\partial x_j} - 2\epsilon_{ijk}\Omega_j u_k. \tag{10}$$

A generalized vorticity equation is derived by taking the curl of Equation 10, that is, $\epsilon_{pqi}\,\partial(10)/\partial x_q$:

$$\frac{D\omega_p}{Dt} = -\underbrace{\epsilon_{pqi}\frac{\partial u_j}{\partial x_q}\frac{\partial u_i}{\partial x_j}}_{1} - \underbrace{\epsilon_{pqi}\frac{1}{\rho^2}\frac{\partial \rho}{\partial x_q}\frac{\partial p}{\partial x_i}}_{2} + \underbrace{\epsilon_{pqi}\frac{\partial}{\partial x_q}\left(\frac{1}{\rho}\frac{\partial \tau_{ij}}{\partial x_j}\right)}_{3} - \underbrace{2\epsilon_{pqi}\epsilon_{ijk}\frac{\partial(\Omega_j u_k)}{\partial x_q}}_{4}, \tag{11}$$

where the relative vorticity vector is defined as $\omega_p = \epsilon_{pqi}\partial u_i/\partial x_q$. Equation 11 states that following the motion of a fluid parcel of unit volume, the rate of change of relative vorticity depends upon:

1. Interaction of velocity shear components (tilting term);

2. Local baroclinicity (solenoidal term);

3. External torques from the curl of the surface stress; and,

4. Planetary vorticity associated with Coriolis acceleration.

c. Application to geophysical flows

1) MECHANICAL ENERGY

In analyzing the evolution of geophysical fluids, the effects of stratification and rotation must be taken into account. Considering the energy budget within the upper ocean, it has been shown that rotation effects are non-existent since the Coriolis acceleration always acts normal to the direction of flow. The Coriolis acceleration's indirect influence will not be completely eliminated however, since it provides a convenient

limiting timescale for the evolution of certain relevant flows, such as near-inertial currents, which will be examined later. The effect of the ocean's stratification does, however, directly enter the problem, allowing some simplifying assumptions to be made.

First, a coordinate system is defined such that the direction of the gravity vector defines the vertical, and is directed opposite. Thus, $i = 3$ in the body force term and, since it is a repeated index, the only term that survives is $-\rho g w$, with $w = u_3$ (i.e. the vertical component of velocity). With the definition that $Dz/Dt \equiv w$, and assuming constant gravitational acceleration, the work done by the body force can be expressed in terms of the rate of change of geopotential $\Phi = gz$:

$$\rho u_i g_i = -\rho \frac{D\Phi}{Dt}. \tag{12}$$

When moved over to the left side of the mechanical energy equation, it is clear that this term represents an exchange of KE with potential energy (PE) through motion across a geopotential surface.

Stratification affects the geometry of the volume under consideration by constraining its vertical scale H relative to the horizontal scale L, such that $H/L \ll 1$. By examining the incompressible approximation to the continuity equation:

$$\frac{\partial u_j}{\partial x_j} = \frac{\partial u}{\partial x} + \frac{\partial v}{\partial y} + \frac{\partial w}{\partial z} = 0, \tag{13}$$

and choosing scales for the horizontal length $L = (x, y)$, horizontal velocity $U = (u, v)$, and vertical velocity W, it may be seen that:

$$W \simeq \frac{H}{L} U, \tag{14}$$

or $W \ll U$. This large inequality is also borne out from scaling the vertical component of the momentum equation, and is representative of a fluid in approximate hydrostatic equilibrium. Given the fact that OML depths are typically on the order of tens of meters, and TCs extend tens to hundreds of kilometers

horizontally, this inequality is practically guaranteed. Under this approximation, the KE per unit mass can now be written as $k = (u^2 + v^2)/2$. Additionally, with horizontal and vertical gradient scales defined as H^{-1} and L^{-1}, respectively, the vertical gradient scale is clearly much greater. With this assumption, $j = 3$ in the surface energy flux term, and $i = (1, 2)$ is repeated, allowing the approximation:

$$\begin{aligned} \frac{\partial(u_i \tau_{ij})}{\partial x_j} &\simeq \left[\frac{\partial(u\tau_{xz})}{\partial z} + \frac{\partial(v\tau_{yz})}{\partial z}\right] \\ &\simeq \frac{\partial(\vec{u} \cdot \vec{\tau})}{\partial z} \end{aligned} \tag{15}$$

to be made. The horizontal velocity and stress vectors are denoted as $\vec{u}$ and $\vec{\tau}$, respectively. From this point forward, vector notation will be used to denote operations on quantities in the horizontal spatial dimensions, and tensor notation will be retained for general spatial operations.

Similarly, the viscous dissipation term can be approximated as:

$$2\mu \left(\frac{\partial u_i}{\partial x_j}\right)^2 \simeq 2\mu \left[\left(\frac{\partial u}{\partial z}\right)^2 + \left(\frac{\partial v}{\partial z}\right)^2\right]. \tag{16}$$

The mechanical energy equation under the assumptions summarized thus far is:

$$\rho \frac{Dk}{Dt} = -\rho g w + p\frac{\partial u_j}{\partial x_j} + \frac{\partial(\vec{u} \cdot \vec{\tau})}{\partial z} - \epsilon, \tag{17}$$

where $\epsilon \equiv 2\mu[(\partial u/\partial z)^2 + (\partial v/\partial z)^2]$.

The Boussinesq approximation is now invoked, which is applicable to situations where perturbations to the mass distribution are small in comparison to a background basic state, and accordingly, compressibility effects are negligible. The total density and pressure fields are written as $\rho = \rho_0 + \rho'(z)$ and $p = p_0(z) + p'(x, y, z)$, respectively, where (ρ_0, p_0) are the basic state quantities and the primes indicate perturbations

to the basic state. The perturbations are defined to be small relative to the basic state, such that $\rho' \ll \rho_0$ and $p' \ll p_0$. The basic state is assumed to be in hydrostatic equilibrium:

$$\frac{\partial p_0}{\partial z} = -\rho_0 g. \tag{18}$$

After some algebra, substituting these relations into the mechanical energy equation allows the replacement of the total density by the basic state, except where coupled to the work done by the body force. Additionally, the work done by volume changes is coupled with the perturbation pressure. Under the Boussinesq approximation the mechanical energy equation is:

$$\rho_0 \frac{Dk}{Dt} = -\rho' g w + p' \frac{\partial u_j}{\partial x_j} + \frac{\partial(\vec{u} \cdot \vec{\tau})}{\partial z} - \epsilon. \tag{19}$$

The reversible KE exchange with internal energy is associated with the term $p' \partial u_j / \partial x_j$, and states that work is done on the volume through compression of the volume. Therefore, under the assumption of incompressibility ($\partial u_j / \partial x_j = 0$), this term does not contribute to the energy budget. It is explicitly retained, however, since it states that the volume is conserved, meaning the depth-integrated horizontal divergence of fluid must be compensated by a change in the depth of the volume. This term represents changes in the depth of the OML due to the oscillatory pattern of upwelling (downwelling) forced by the divergence (convergence) of near-inertial currents typically observed to the rear of a traveling storm (e.g. as simulated by Chang and Anthes (1978) and observed by Shay et al. (1989, 1990)).

Finally, the total rate of KE change per unit mass may be separated into its local and advective changes by defining:

$$\frac{Dk}{Dt} \equiv \frac{\partial k}{\partial t} + \frac{\partial(k u_j)}{\partial x_j}. \tag{20}$$

After substituting these geophysical approximations into the mechanical energy equation, a "working" equation can be derived:

$$\underbrace{\frac{\partial(\rho_0 k)}{\partial t}}_{1} = -\underbrace{\frac{\partial(\rho_0 k u_j)}{\partial x_j}}_{2} - \underbrace{\rho' g w}_{3} + \underbrace{p' \frac{\partial u_j}{\partial x_j}}_{4} + \underbrace{\frac{\partial(\vec{u}\cdot\vec{\tau})}{\partial z}}_{5} - \underbrace{\epsilon}_{6}. \tag{21}$$

The terms in the above expression represent:

1. Local rate of change of KE density;
2. Net transport of KE into or out of the volume;
3. Rate of work done by the buoyancy force;
4. Rate of work done by volume changes;
5. Net flux of KE into or out of volume by surface stresses; and,
6. Dissipation of KE by viscous forces.

2) VORTICITY EQUATION

As was done for the energy budget equation, the upper ocean is assumed to be in approximate hydrostatic equilibrium, such that the vertical component of the momentum equation (Equation 10 with $i = 3$) reduces to a simple balance between the body force and pressure gradient force. The result is that after taking the curl of the momentum equation, the only component that survives is the vertical component of relative vorticity (Equation 11 with $p = 3$). The relative vorticity can then simply be expressed as a scalar quantity by $\omega_3 = \zeta = (\partial v/\partial x - \partial u/\partial y)$.

Under the Boussinesq approximation, the density ρ is replaced by a mean background value ρ_0 in all terms except for the buoyancy force term in the vertical momentum equation. In the equation for the vertical component of relative vorticity, the solenoidal term contains gradients of (horizontally homogeneous) mean density. Thus, under the Boussinesq approximation, the solenoidal term does not directly contribute to changes in the vertical component of relative vorticity. This will have consequences when comparing Boussinesq-approximated observations with primitive equation model results, since horizontal variations in the temperature and density fields do in fact exist.

The planetary vorticity has already been simplified somewhat by only considering the vertical component of relative vorticity. Setting $p = 3$ and summing over all repeated indicies in the surviving terms, the planetary vorticity term is:

$$-2\epsilon_{3qi}\epsilon_{ijk}\frac{\partial(\Omega_j u_k)}{\partial x_q} = \\ -2\left(-w\frac{\partial\Omega_1}{\partial x} - \Omega_1\frac{\partial w}{\partial x} + u\frac{\partial\Omega_3}{\partial x} + \Omega_3\frac{\partial u}{\partial x} + w\frac{\partial\Omega_2}{\partial y} + \Omega_2\frac{\partial w}{\partial y} - v\frac{\partial\Omega_3}{\partial y} - \Omega_3\frac{dv}{dy}\right). \tag{22}$$

Under the hydrostatic approximation, $w \ll (u, v)$. Also, it is recognized that Ω_3 only varies in the meridional direction on a rotating sphere. The Coriolis parameter is defined as $f = 2\Omega_3$, with $\Omega_3 = |\Omega| \sin\phi$ for latitude ϕ. Under this set of assumptions, the planetary vorticity contribution is approximated as:

$$-2\epsilon_{3qi}\epsilon_{ijk}\frac{\partial(\Omega_j u_k)}{\partial x_q} = -f\left(\frac{\partial u}{\partial x} + \frac{\partial v}{\partial y}\right) - v\frac{\partial f}{\partial y}, \tag{23}$$

which reveals the important large-scale geophysical property that changes in relative vorticity are due to both convergence of the horizontal flow (stretching) and meridional excursions of parcels (β-effect). As is customary in geophysical fluid studies, the Coriolis parameter is expanded in a Taylor series about a

central latitude ϕ_0:

$$f = f_0 + \beta y + O(y^2) + ..., \tag{24}$$

where the meridional gradient of planetary vorticity at ϕ_0 is:

$$\beta \equiv \left(\frac{df}{dy}\right)_{\phi_0} = \left(\frac{\partial f}{\partial \phi}\frac{\partial \phi}{\partial y}\right)_{\phi_0} = \frac{2|\Omega|\cos\phi_0}{a}, \tag{25}$$

a is the radius of the earth ($\simeq$ 6370 km). Under the traditional mid-latitude β-plane approximation, terms of order 2 and greater are neglected, and $f_0 \gg \beta y$.

Individual components of the tilting term are examined by setting $p = 3$ as before and summing over repeated indices:

$$\epsilon_{3qi}\frac{\partial u_j}{\partial x_q}\frac{\partial u_i}{\partial x_j} = \left[\frac{\partial u}{\partial x}\frac{\partial v}{\partial x} + \frac{\partial v}{\partial x}\frac{\partial v}{\partial y} + \frac{\partial w}{\partial x}\frac{\partial v}{\partial z} - \frac{\partial u}{\partial y}\frac{\partial u}{\partial x} - \frac{\partial u}{\partial y}\frac{\partial v}{\partial y} - \frac{\partial w}{\partial y}\frac{\partial u}{\partial z}\right]. \tag{26}$$

Equation 26 can be combined into two terms consisting of a relative vorticity contribution and a contribution due to shear:

$$\epsilon_{3qi}\frac{\partial u_j}{\partial x_q}\frac{\partial u_i}{\partial x_j} = \zeta(\nabla \cdot \vec{u}) + \left(\frac{\partial w}{\partial x}\frac{\partial v}{\partial z} - \frac{\partial w}{\partial y}\frac{\partial u}{\partial z}\right). \tag{27}$$

The first term on the right-hand side represents a stretching mechanism which is analogous to the divergence term in the energy equation. Implicit in this term is the relationship between upwelling of the thermocline and an increase in vorticity within the OML column, as will be shown later. The second term on the right-hand side represents relative vorticity exchanges among the three components of the general vorticity vector.

Finally, the surface stress term is simplified analogous to the surface energy flux term, due to the vertical gradient scale being much larger than the horizontal. With these approximations, and splitting

the total derivative into local and advective contributions, the equation for local rate of change of relative vorticity becomes:

$$\underbrace{\frac{\partial \zeta}{\partial t}}_{1} = \underbrace{-\frac{\partial(\zeta u_j)}{\partial x_j}}_{2} \underbrace{-(\zeta + f_0)(\nabla \cdot \vec{u})}_{3} \underbrace{-\beta v}_{4} \underbrace{-\left(\frac{\partial w}{\partial x}\frac{\partial v}{\partial z} - \frac{\partial w}{\partial y}\frac{\partial u}{\partial z}\right)}_{5} + \underbrace{\frac{1}{\rho_0}\frac{\partial}{\partial z}\left[\mathbf{k} \cdot (\nabla \times \vec{\tau})\right]}_{6}. \quad (28)$$

The terms in the above expression represent:

1. Local rate of change of relative vorticity;
2. Net transport of relative vorticity into or out of the volume;
3. Vortex stretching due to divergence;
4. Changes in vorticity from meridional motion;
5. The “twisting” term which exchanges vorticity among components; and,
6. The divergence of the curl of the surface stress.

d. Application to the OML

It is of interest for this research to examine the effects of a cyclone’s forcing on the mean energy and current response within the OML. Typically, the thermodynamic state variables and currents are observed to be approximately constant across the depth of the OML, due to enhanced turbulent mixing processes. For this research, the vertical average of a variable within the OML is defined as:

$$\overline{\phi} = \frac{1}{h}\int_{-h}^{0} \phi \, dz, \quad (29)$$

where $\phi = (u, v, T, S, k, \zeta)$, and h is the depth of the OML. The overline will be dropped from the vertically-averaged variables, with the understanding that a mean OML quantity is intended.

1) VOLUME CONSERVATION

Referring back to Equation 13, the continuity equation may be vertically integrated over the depth of the OML to obtain:

$$h\left(\frac{\partial u}{\partial x} + \frac{\partial v}{\partial y}\right) + w|_{-h} - w|_0 = 0. \tag{30}$$

The sea surface is assumed to be a rigid lid, which eliminates barotropic disturbances. Observations indicate that the ocean's current response to a TC is primarily baroclinic in nature, particularly in the deep ocean (Shay et al. 1990), so the rigid-lid approximation is reasonable. Under this assumption, $w(z = 0) = 0$. The upwelling at the OML base is:

$$w|_{-h} = \frac{Dh}{Dt} = \frac{\partial h}{\partial t} + \vec{u} \cdot \nabla h, \tag{31}$$

and the vertically integrated continuity equation for the OML becomes:

$$\frac{\partial h}{\partial t} = -\nabla \cdot (h\vec{u}), \tag{32}$$

which states that the horizontal mass convergence (divergence) within the OML deepens (shoals) the OML. If the amplitude of the change in OML depth is small compared to the wavelength, Equation 32 may be linearized to obtain the simplified expression:

$$\frac{\partial h}{\partial t} = -h(\nabla \cdot \vec{u}). \tag{33}$$

2) MECHANICAL ENERGY EQUATION

The OML has been assumed to be well-mixed in mass and momentum, and therefore internal dissipative processes are removed ($\epsilon = 0$) when integrated over the OML depth. The vertically-integrated mechanical energy equation is:

$$\begin{aligned} \rho_0 h \frac{\partial k}{\partial t} &= -\rho_0 h \nabla \cdot (k\vec{u}) - \frac{\rho' g}{2} \frac{\partial (h^2)}{\partial t} + p' \left[h(\nabla \cdot \vec{u}) + \frac{\partial h}{\partial t} \right] \\ &\quad + \vec{u} \cdot \vec{\tau}|_0 - \vec{u} \cdot \vec{\tau}|_{-h}, \end{aligned} \tag{34}$$

where the integrated continuity equation has been substituted into the pressure work term. The primed quantities represent the stratification "jumps" at the OML base. Equation 34 is identical to the energy equation (Equation 6) in Price (1983), with the addition here of the explicit stress term at the OML base to represent mixing processes. For comparison, Jacob et al. (2000) include this mixing term in the expression of conservation of mass within the OML, but the overall effect on the energy balance within the OML is the same. Thus, exchanges of KE with PE (i.e. changes in OML depth) are associated with two separate processes, the first a result of the change in depth due to stress-driven turbulent motions, and the second due to divergence of the horizontal current and volume conservation requirements. The depth-integrated mechanical energy equation is now expressed symbolically as:

$$k_t = -E_A - E_B + E_P + E_W - E_M, \tag{35}$$

where k_t represents the rate of change per unit area of KE, and right hand side forcing terms are: E_A, the advection of KE; E_B, the exchange of KE with PE due to motions across geopotential surfaces; E_P, due to upwelling (downwelling) motions associated with horizontal divergence (convergence); E_W, the

surface wind forcing; and E_M, the energy flux due to shear stresses at the OML base. This latter term is often overlooked in the energy equation, but has important consequences for OML processes, such as layer deepening and cooling.

3) VORTICITY EQUATION

It is assumed that the momentum and vorticity in the OML are adequately represented by their average, depth-independent, quantities. The vorticity equation (Equation 28) is vertically integrated over the OML to obtain:

$$\begin{aligned} h\frac{\partial \zeta}{\partial t} &= -h\nabla\cdot(\zeta\vec{u}) - h(\zeta+f_0)(\nabla\cdot\vec{u}) - h\beta v \\ &\quad + \frac{1}{\rho_0}\left[\mathbf{k}\cdot(\nabla\times\vec{\tau})\right]_0 - \frac{1}{\rho_0}\left[\mathbf{k}\cdot(\nabla\times\vec{\tau})\right]_{-h}. \end{aligned} \tag{36}$$

The twisting terms are removed since they involve vertical shears of the horizontal current. The vorticity budget equation is re-written in a compact symbolic form as:

$$\zeta_t = -V_A - V_S - V_B + V_W - V_M, \tag{37}$$

where ζ_t is the local rate of change of relative vorticity, and the right-hand side forcing terms are: V_A, advective transport of relative vorticity into or out of the OML; V_S, vorticity stretching from the divergence of the horizontal current; V_B, the β term, where relative vorticity is changed from meridional motions; V_W, the wind stress curl; and V_M the curl of the surface stress at the OML base.

e. Scale analyses

1) MECHANICAL ENERGY EQUATION

To analyze the relative contributions of the forcing terms in the mechanical energy budget, Equation 35 is non-dimensionalized by introducing scaling parameters for each of the variables. A summary of the dimensional scaling variables is shown in Table 1.

Scale Parameter	*Symbol*
Length	L
Time	f^{-1}
Depth	H
Current speed	U
Kinetic energy per mass	U^2
Background ocean density	ρ_0
Perturbation ocean density	ρ
Perturbation ocean pressure	p
Wind stress	T
Current speed perturbation	u
OML base shear stress	$\rho_0 u^2$
Planetary radius	R

Table 1: Summary of dimensional scaling parameters relevant to analysis of the mechanical energy budget of the OML in response to a moving TC.

Because the Coriolis force does not supply or remove energy from the closed system, its effects do not directly impact the energy problem. This is not to imply that rotation can be totally eliminated however. Since storm-generated currents are observed to be primarily near-inertial in nature (Shay et al. 1992), an inertial timescale (f^{-1}) is important to the problem, where $f = 2|\Omega| \sin\phi$ is the Coriolis parameter at latitude ϕ. Thus, rotation will indirectly enter the problem from a scaling perspective.

Each of the variables is non-dimensionalized in terms of its scale value and substituted into the verti-

cally integrated mechanical energy equation. The scaled form of Equation 35 becomes:

$$\begin{aligned} k_t' \left[\rho_0 U^2 H f\right] &= -E_A' \left[\frac{\rho_0 U^3 H}{L}\right] - E_B' \left[\rho g H^2 f\right] + E_P' \left[\frac{\rho g H^2 U}{L}\right] \\ &\quad + E_W' \left[UT\right] - E_M' \left[U \rho_0 u^2\right], \end{aligned} \tag{38}$$

where the primed quantities represent non-dimensional terms, and dimensional scales are in brackets. In the above expression, it has been assumed that the pressure perturbations are themselves in hydrostatic balance, so that $p = \rho g z$ has been substituted. This approximation is acceptable under conditions of weak vertical transports (e.g. convective or Langmuir circulations).

Since relative contributions of the forcing terms to the change in OML KE are sought, the scaling terms are non-dimensionalized by dividing through by the local KE tendency scale $(\rho_0 U^2 H f)$ such that the local change is of unit order:

$$\begin{aligned} k_t' \left[1\right] &= -E_A' \left[\frac{U}{fL}\right] - E_B' \left[\frac{g' H}{U^2}\right] + E_P' \left[\frac{g' H}{U^2}\frac{U}{fL}\right] \\ &\quad + E_W' \left[\frac{T}{\rho_0 U f H}\right] - E_M' \left[\frac{u^2}{U^2}\frac{U}{fL}\frac{L}{H}\right], \end{aligned} \tag{39}$$

where $g' = \rho g / \rho_0$ is a reduced gravity proportional to the stratification at top of the thermocline. The scales can now be expressed in terms of more familiar non-dimensional coefficients. A table of those numbers relevant to the problem are shown in Table 2.

Coefficient	*Symbol*
Rossby number	$\mathrm{Ro} = U/fL$
Froude number	$\mathrm{Fr} = U^2/g'H$
Burger number	$\mathrm{Bu} = \mathrm{Ro}/\mathrm{Fr}$
Ekman number	$\mathrm{Ek} = T/\rho_0 U f H$
OML aspect ratio	$\delta = H/L$
Non-dim. KE	$\mathrm{K} = u^2/U^2$

Table 2: Non-dimensional coefficients of the OML mechanical energy balance equation.

Substitution of these coefficients into the non-dimensional energy equation (Equation 39) gives:

$$k'_t = \mathrm{Ro}\, E'_A - \frac{1}{\mathrm{Fr}}\, E'_B + \mathrm{Bu}\, E'_P + \mathrm{Ek}\, E'_W - \frac{\mathrm{K\,Ro}}{\delta}\, E'_M. \tag{40}$$

The Rossby number reflects the importance of non-linear forcing, and for large-scale ocean dynamics, is typically $O(10^{-2})$ or smaller, but on the mesoscale may be significantly larger. The Froude number expresses the exchange of KE with PE; when large, relatively little KE is lost since stratification is weak. The Ekman number is expected to be large under strong surface forcing such as a TC. The Richardson number, which is typically the basis for parameterizing the turbulent flux of energy out of the OML, can be formed from the Froude number and non-dimensional KE ($\mathrm{Ri}^{-1} = \mathrm{Fr\,K}$). It has been suggested (Price 1981) that Bu is proportional to the frequency shift of the near-inertial current oscillation above the local inertial frequency. Shay et al. (1998) found this to be approximately true based on observations in Hurricane Gilbert.

2) VORTICITY BUDGET

Analogous to the scaling of the mechanical energy budget, the vorticity equation (Equation 37) is non-dimensionalized in terms of dimensional scaling parameters. Two additional scales appear to those shown in Table 1 concerning the energy equation. These are the planetary radius R and the "beta" parameter ($\beta = f/R$).

The dimensional scaled form of the vorticity equation integrated over the OML depth is:

$$\zeta'_t \left[\frac{UfH}{L}\right] = -V'_A \left[\frac{U^2 H}{L^2}\right] - V'_S \left[\frac{HfU}{L}\right] - V'_B \left[\frac{HfU}{R}\right] + V'_W \left[\frac{T}{\rho_0 L}\right] - V'_M \left[\frac{\rho_0 u^2}{\rho_0 L}\right], \tag{41}$$

where, as before, primes indicate the non-dimensionalized terms in the vorticity equation. In the stretching term, it has been assumed that the absolute vorticity scales as $f \geq U/L$, which insures that inertial oscillations remain stable. A non-dimensional form is obtained by dividing Equation 41 through by the relative vorticity local tendency scale UfH/L:

$$\zeta_t'[1] = -V_A' \left[\frac{U}{fL}\right] - V_S'[1] - V_B' \left[\frac{L}{R}\right] + V_W' \left[\frac{T}{\rho_0 U f H}\right] - V_M' \left[\frac{u^2}{U^2}\frac{U}{fL}\frac{L}{H}\right]. \tag{42}$$

Substitution of the relevant non-dimensional parameters defined in Table 2, Equation 42 can be rewritten as:

$$\zeta_t' = -\mathrm{Ro}\, V_A' - 1\, V_S' - P\, V_B' + \mathrm{Ek}\, V_W' - \frac{\mathrm{K\,Ro}}{\delta}\, V_M'. \tag{43}$$

The additional non-dimensional parameter $P = L/R$ appears in the vorticity equation. Since typically $P \ll 1$ for mesoscale motions, the β-term can safely be removed from the problem, which effectively filters out Rossby waves.

4. Observations and Preliminary Analyses

During the 2002 NOAA Hurricane Research Division's hurricane field program, a joint NOAA/NSF experiment was designed to measure both the kinematic and thermodynamic upper-ocean response to a propagating mature tropical cyclone. The experiment consisted of a series of research flights, each deploying expendable probes in the same location before, during, and after passage of the cyclone. A set of pre-storm flights were conducted from 18-23 Sept. 2002, the in-storm flight occurred on 02 Oct., and a final post-storm survey was made on 04 Oct. The large set of ocean observations included both *in situ* and remotely-sensed data. Among the data obtained, relevant observations included an array of current and temperature profiles from Airborne Expendable Current Probes (AXCP), temperature and salinity profiles from Airborne Expendable Conductivity-Temperature-Depth (AXCTD) probes, temperature profiles from Airborne Expendable Bathythermograph (AXBT), and surface directional wave spectra from the NASA SRA. The surface wind field was measured from observations by GPS dropwindsondes and the HRD SFMR.

a. In-storm atmospheric data

Each of the NOAA P-3 aircraft operates an SFMR, which estimates the surface wind speed along the fight track. The SFMR measures winds based on the theory of increased blackbody radiation from sea foam. The accuracy of surface winds measured by the SFMR has been documented by Uhlhorn and Black (2003). A time series of surface wind speeds measured by the SFMR along the flight track for each of the flight legs is shown in Figure 1, and Table 3 summarizes the center locations identified from surface wind speed minima and the associated storm motion vector.

In addition, 41 Global Positioning System (GPS) dropwindsonde (Hock and Franklin 1999) 10 m

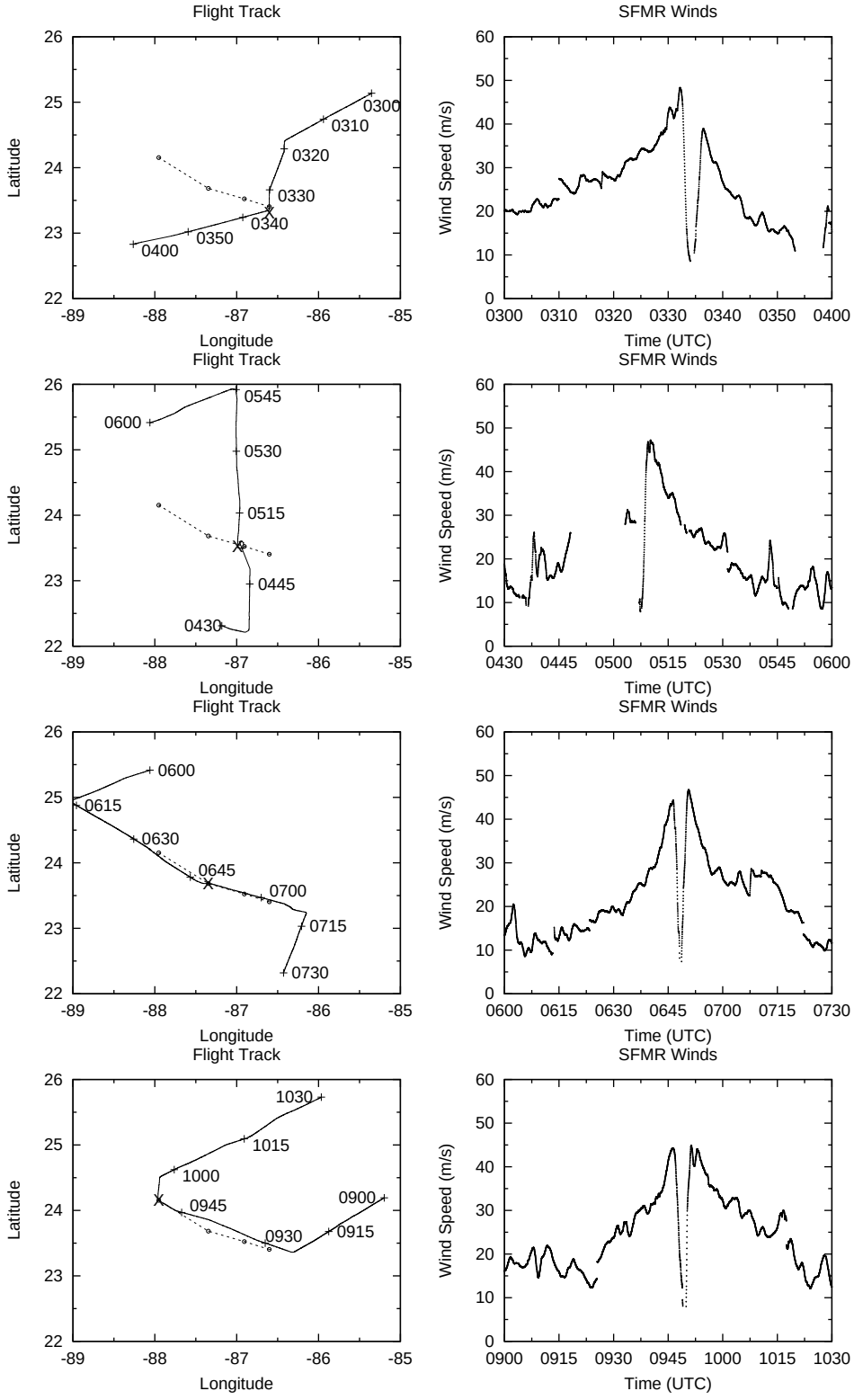

Figure 1: Surface wind speed measured by the SFMR along four segments of the flight track during the 02 October 2002 in-storm flight in Lili. In the left panels, the 'X' marks the approximate location of the center of Lili and the open circles/dashed line indicates the storm track and locations of the center at each of the four passes through the eye. Note that a large data gap exists from around 0450 to 0505 UTC. The peak 1-min average wind speed of 49 $\mathrm{m\,s^{-1}}$ was found on the north side of the storm.

Time (UTC)	*Lat.* (°)	*Lon.* (°)	*Spd.* ($\mathrm{m\,s^{-1}}$)	*Head.* (°)
0334	23.405	-86.602		
			7.4	288.5
0507	23.523	-86.987		
			6.6	296.0
0649	23.683	-87.345		
			7.4	310.2
0950	24.153	-87.952		

Table 3: Summary of center locations estimated from the wind speed minima in the SFMR measurements shown in Figure 1. The storm motion vector (speed and heading) computed from the centers is also indicated. The average motion over the observation time is 7 $\mathrm{m\,s^{-1}}$ at 292° from true north.

wind vector measurements are available, as well as occasional data buoy wind reports. All collected wind measurements are analyzed in a common framework (space and time averaging characteristics) with the Hurricane Research Division's H*WIND surface wind analysis system (Powell et al. 1998). The result is a user-defined resolution gridded field of 10-m height wind vectors in a storm-relative coordinate system. The objectively-analyzed surface wind field of Hurricane Lili on 02 October is shown in Figure 2.

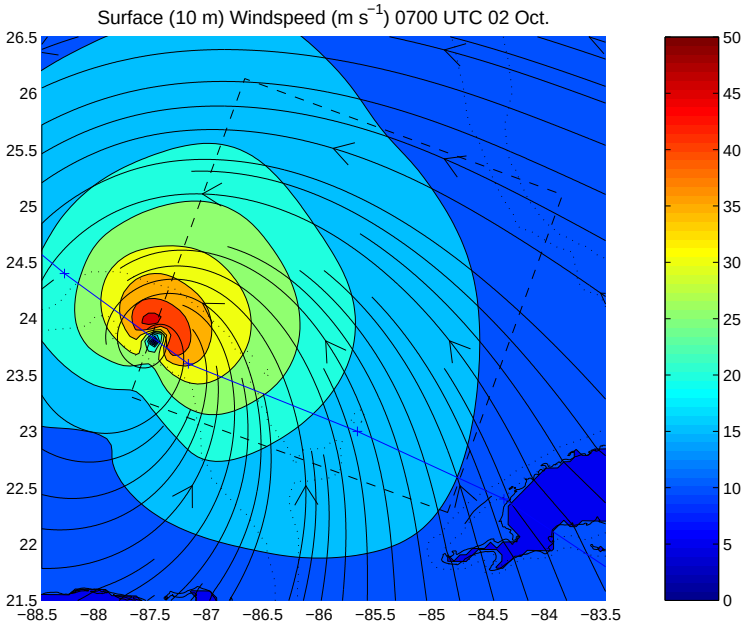

Figure 2: H*WIND surface wind analysis of Hurricane Lili on 02 October 2002 at 0700 UTC. Isotachs are contoured every 5 $\mathrm{m\,s^{-1}}$. Data used to generate this analysis include observations from SFMR, GPS dropwinsondes, QuikSCAT scatterometer, and available hourly buoy reports. The storm track is indicated by the solid line, and the dashed box shows the ocean data analysis region considered for this research.

GPS sondes also measure the thermodynamic atmospheric profile (temperature, pressure, and moisture) from flight-level down to the sea surface. Though not central to the theme of this work, the surface fluxes of sensible and latent heat within the storm may be estimated from this data. Storm-relative plots of these variables are shown in Figure 3.

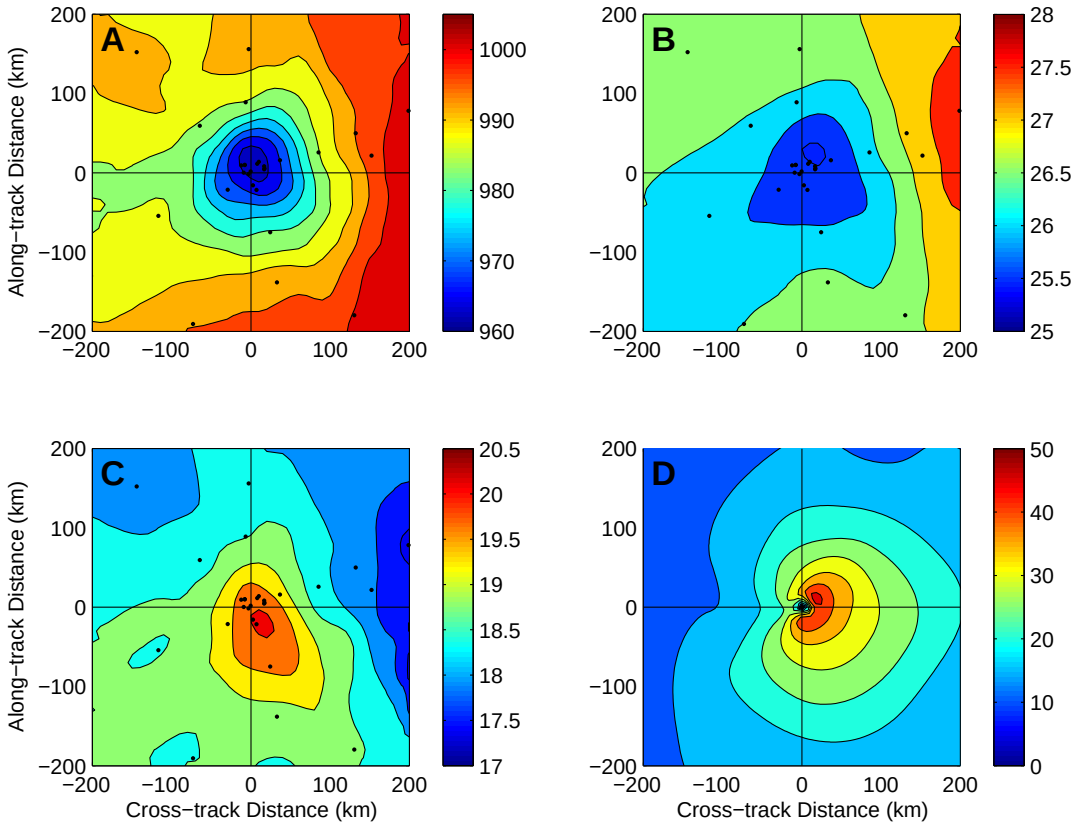

Figure 3: Analyses of surface pressure (A), 10-m temperature (B) and specific humidity (C), and 10-m surface wind analysis (D) shown in Figure 2. Plots are rotated such that the y-axis is aligned with the direction of storm motion, and the origin is at the center of the cyclone.

b. Ocean data

Research flights into Hurricanes Isidore and Lili in 2002 are unprecedented in the volume of upper-ocean data collected. Temperature profiles are measured by all deployed AXBT, AXCP, and AXCTD. The upper-ocean current field is measured by AXCP, and for the first time, salinity by AXCTD. When

combined and objectively analyzed, these data help construct the complete OML kinematic and thermodynamic structure ahead of, within, and behind the storm. Since the earth-relative location of each of the grids is identical, the evolution of the OML response to the storm forcing can tracked. Table 4 summarizes the number of profiles obtained during the series of experiments. Due to faulty compound surrounding the thermistor seals, AXCP temperature profiles are typically not as reliable as currents measurements.

Flight	*AXBT*	*AXCTD (temp.)*	*AXCTD (sal.)*	*AXCP (temp.)*	*AXCP (cur.)*
020918I (Pre)	17 (20)	– (23)	– (23)	– (16)	– (16)
020919I (Pre)	18 (19)	18 (21)	16 (21)	9 (18)	13 (18)
020921I (Pre)	18 (19)	6 (14)	7 (14)	18 (30)	15 (30)
020922H (Pre)	19 (21)	– (–)	– (–)	– (–)	– (–)
020923I (Pre)	14 (21)	13 (16)	11 (16)	9 (27)	15 (27)
021002I (In)	15 (19)	7 (18)	10 (18)	16 (26)	17 (36)
021004I (Post)	14 (18)	17 (18)	17 (18)	24 (35)	31 (35)
Total	105 (137)	61 (110)	61 (110)	76 (152)	91 (152)

Table 4: Summary of ocean probe deployments during the series of research flights in Hurricanes Isidore and Lili. The flight ID is given as date, and 'H' or 'I' identifies the aircraft. In the number columns, the number of profiles used for this research is listed first, and the total number deployed is listed in parenthesis.

The profile measured by AXCP contains the total current consisting of a mean and a perturbation as well as contributions from orbital velocities induced by low frequency surface waves. Prior to the objective analysis, orbital velocties are removed from the profiles using the least-squares method of Sanford et al. (1982) and applied to similar data (Shay et al. 1989, 1992).

1) PRE-STORM

Grids of ocean probes were deployed from 18 to 23 September to estimate the initial pre-storm conditions for Hurricane Isidore, based on the forecasted storm track. In addition to generally estimating the initial conditions, the deployment strategy was designed to target regions of oceanic mesoscale variability (the Gulf of Mexico Loop Current) to assess the role of these features on the TC's intensity change pro-

cess. Isidore's actual track deviated significantly to the south of the forecast, traveling almost due west off of the western tip of Cuba toward the northern Yucatan peninsula. Hurricane Lili did however traverse the grid of data approximately one week later. The locations of the deployed ocean probes used to estimate the initial OML conditions are shown relative to the track of Lili in Figures 4 through 6.

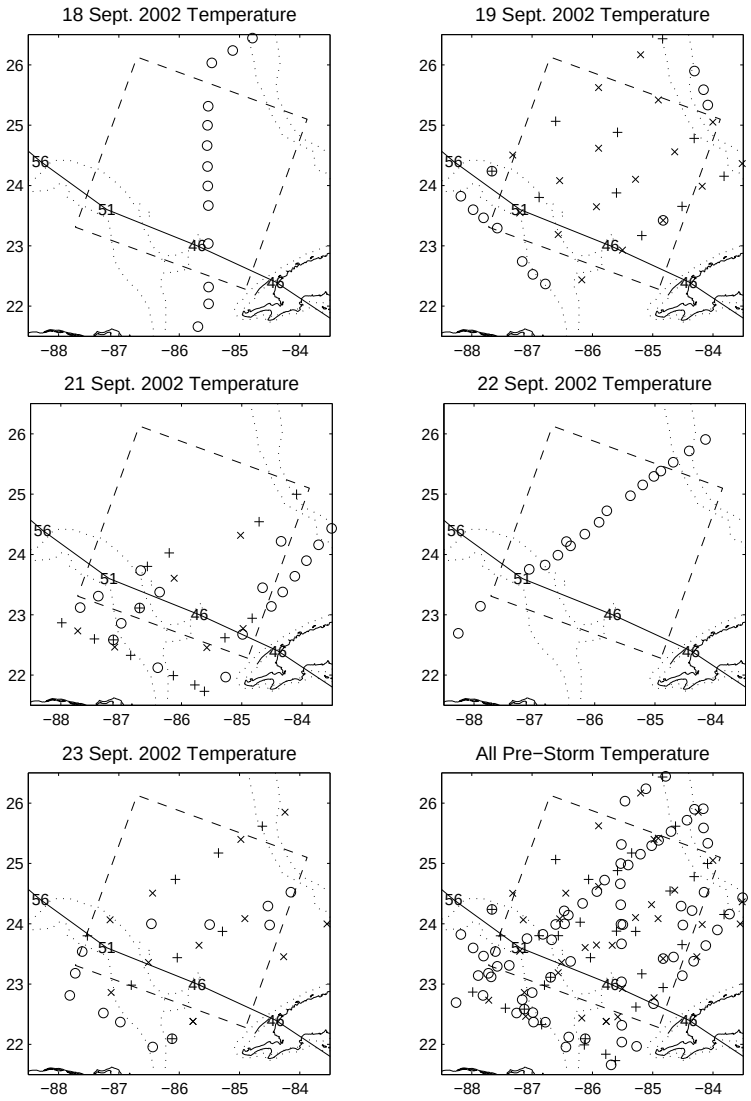

Figure 4: Locations of the ocean probes deployed prior to the passage of Hurricane Lili used to estimate the initial temperature conditions. AXBTs are identified by ($\circ$), AXCTDs by ($\times$), and AXCPs by ($+$). The observed track of Lili is indicated by the solid line, and labeled in six-hour increments by maximum surface wind speed ($\mathrm{m\,s^{-1}}$). The dashed grid box indicates the analysis region, and the dotted contours indicate the 200 m and 1000 m isobaths.

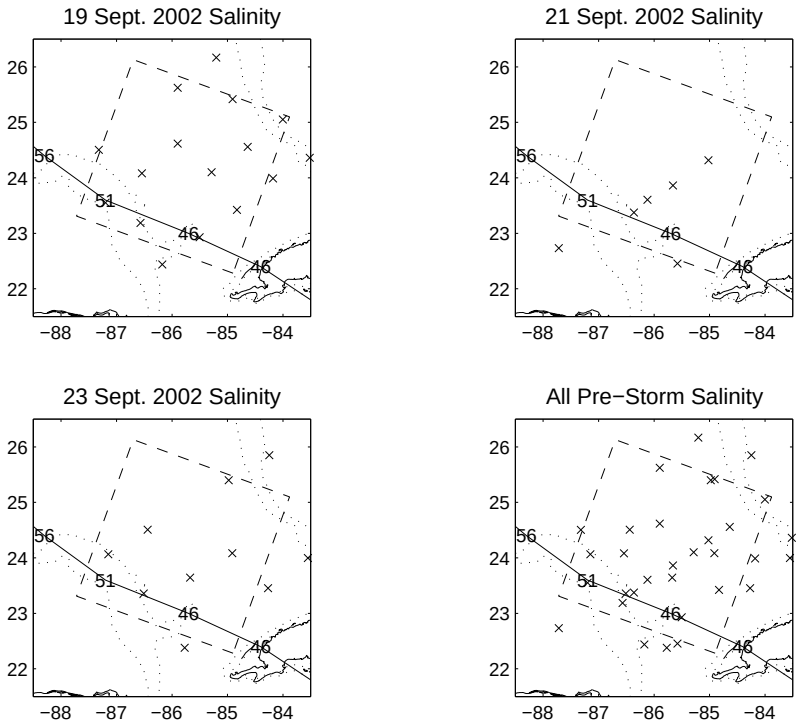

Figure 5: AXCTD locations which measured salinity profiles prior to the passage of Hurricane Lili.

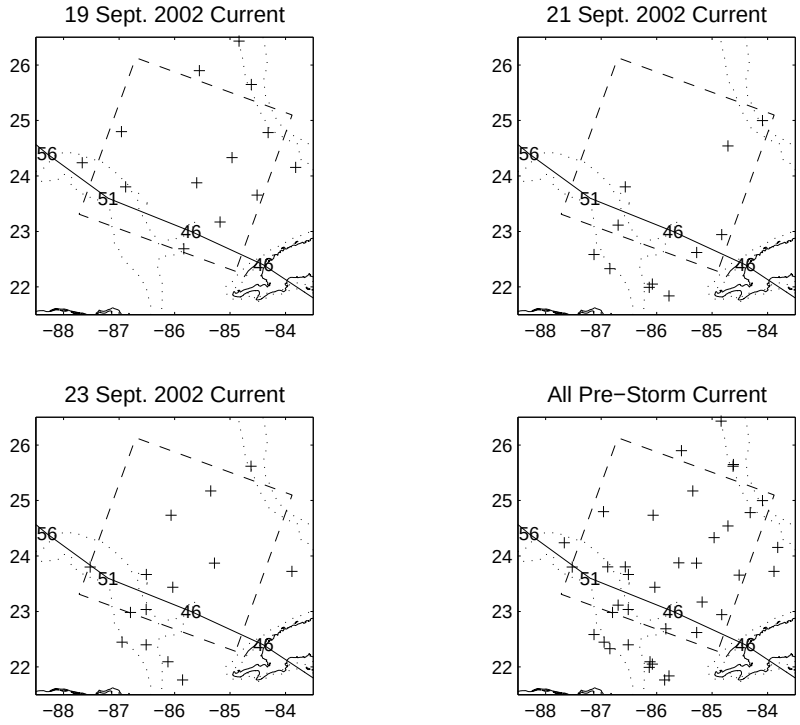

Figure 6: AXCP locations which measured horizontal current profiles prior to the passage of Hurricane Lili.

2) IN-STORM

The observations obtained on 02 October 2002 represent conditions under direct forcing from Hurricane Lili. Locations of the ocean probes deployed during the flight are shown in Figure 7. Data were acquired as Lili was undergoing a period of rapid intensification from Category 2 to Category 4 strength.

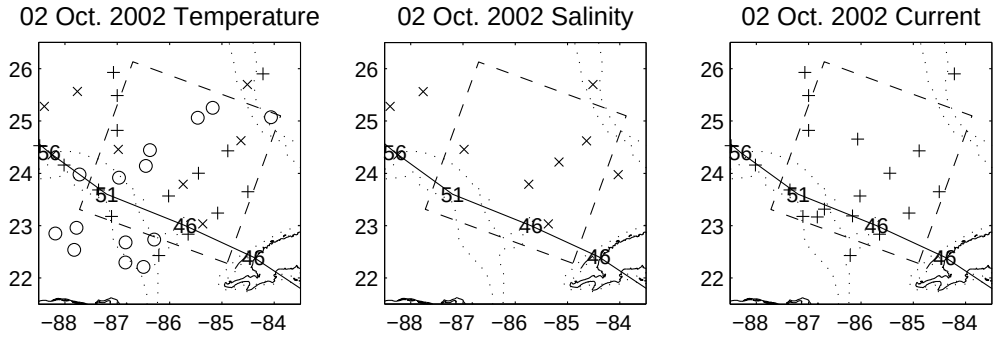

Figure 7: Locations of the ocean probes deployed during the the in-storm research flight pattern in Hurricane Lili on 2 October 2002. Symbols are the same as in Figure 4.

The NASA SRA (Wright et al. 2001) measures the directional sea surface wave spectrum along the flight track using altimetric methods. The SRA operated during the in-storm survey and provided data useful for assessing the role of the swell in modulating the energy flux across the air-sea interface. A time-series of significant wave heights from the SRA along one particular leg of the flight track is shown in Figure 8.

Based on the flight altitude (1800 m) and instrument characteristics, the highest wavenumber resolved by the SRA during the Lili flight is 0.112 $\mathrm{rad\,m^{-1}}$, ($L = 56$ m wavelength), which indicates that the directly forced wind sea ($> \sim 0.2\,\mathrm{rad\,m^{-1}}$ or $L < 30$ m, Hanson and Phillips (1999)) is not resolved. It is believed that the longer wave field does not play a major role in momentum and energy transfers from the wind to the OML (Csanady 2001). There is, however, observational evidence to indicate that the presence of swell can modulate the fluxes depending upon the orientation of the wind direction and propagation direction of the swell (Drennan et al. 1999).

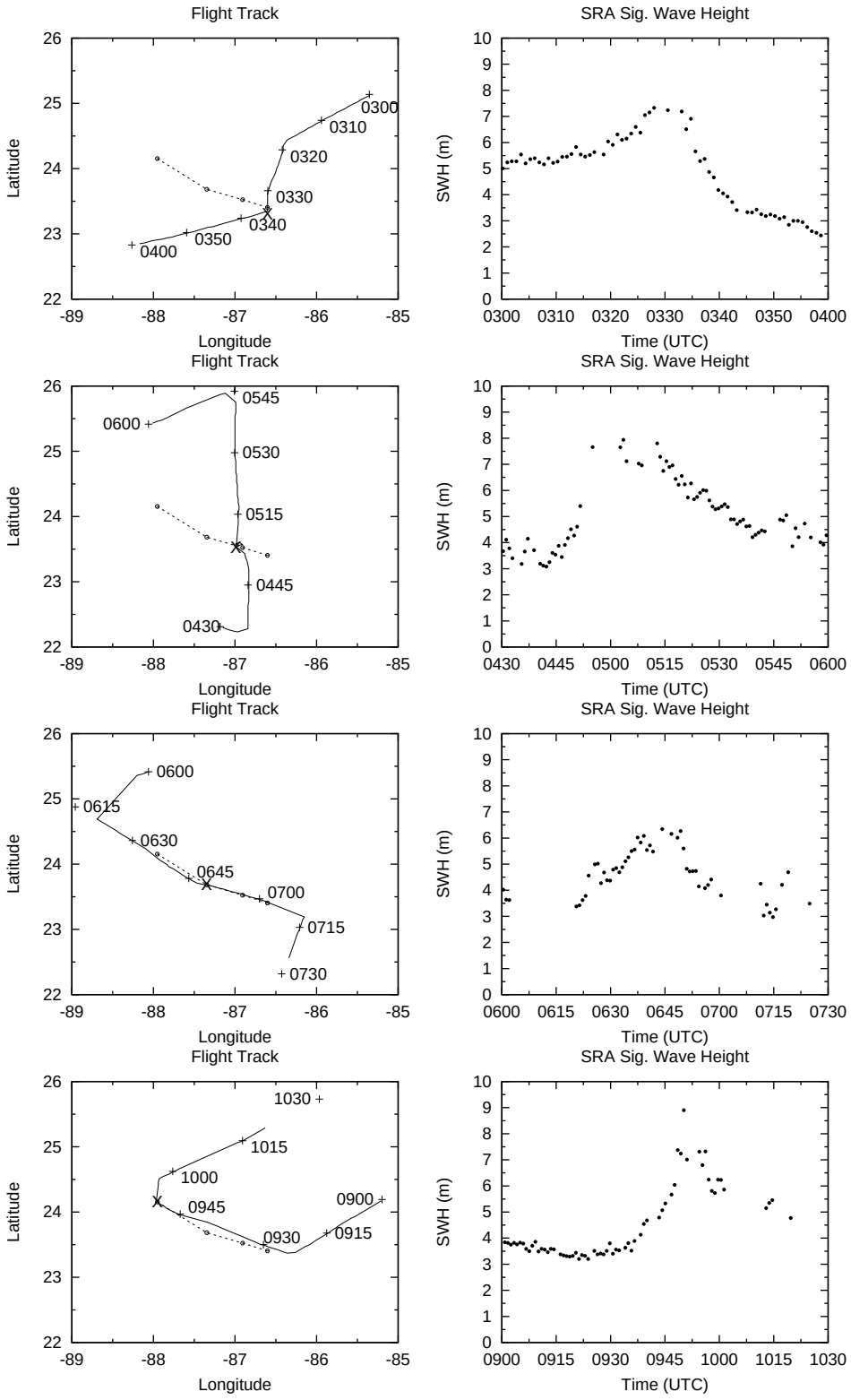

Figure 8: Significant wave height (m) measured by the SRA along four segments of the flight track during the 02 October 2002 in-storm flight in Lili. In the left panels, the 'X' marks the approximate location of the center of Lili and the open circles/dashed line indicates the storm track and locations of the center at each of the four passes through the eye.

3) POST-STORM

The final post-storm research flight was conducted on 04 Oct. 2002 over the same location as the in-storm pattern flown roughly 60 hours prior. Figure 9 shows the locations of the ocean probes deployed during the mission.

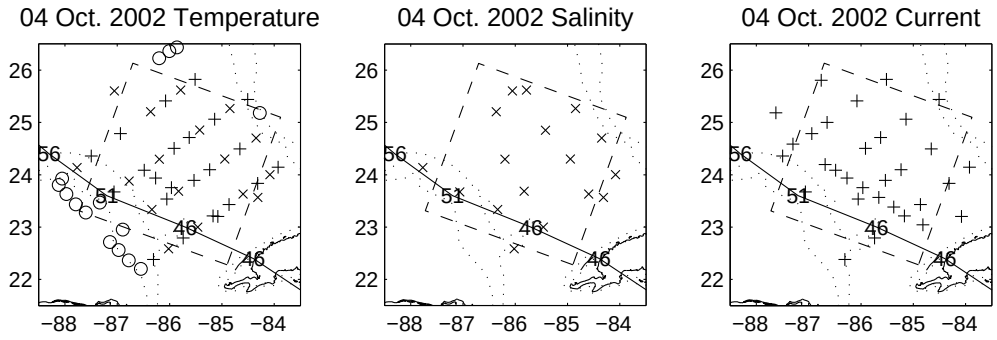

Figure 9: Locations of the ocean probes deployed during the the post-storm research flight on 04 October 2002. Symbols are the same as in Figure 4.

c. Thermodynamic analyses

Based on the observed upper ocean profiles of temperature and salinity, gridded analyses of these quantities are generated. Specifically for this research, it is of primary interest to estimate the mass distribution (density) within and just below the OML. From the analyzed temperature and salinity fields, the density is calculated using the polynomial equation of state for seawater (Millero et al. 1980; Fofonoff and Millard 1983).

Each of the profiles are manually and objectively checked for bad data, and spikes are removed by applying a median filter. The temperature and salinity data are then averaged over layers to compute mean quantities at regular levels. To improve the quality of the observations, as well as to compute an estimate of random noise, average temperatures are computed over 5-m layers for AXBT data, and every 10 m for the AXCTD and AXCP data. Also computed is the standard deviation about the mean value at each point.

In all, the surface value is assumed equal to the first value computed below the surface. For example, the AXBT SST is equal to the mean temperature at 5 m computed from all measurements from between 2.5 and 7.5 m depth.

The objective analysis procedure used for this research is the OAX5 package (Canada Bedford Institute of Oceanography) and is based on the approach of Bretherton et al. (1976). OAX5 uses a linear optimal interpolation technique to estimate values at gridpoints based on observations at nearest neighbors. The interpolation is generalized to allow variable correlation scales in any number of dimensions. The default covariance model implemented in OAX5 and used here is:

$$\mathrm{cov}[d] = \exp(-d) \cdot \left(1 + d + \frac{d^2}{3}\right), \tag{44}$$

where d is the distance between the observation and gridpoint normalized by a user-specified dimensional correlation scale factor. Figure 10 shows the covariance model function plotted as a function of distance based on a unit correlation scaling factor. The analyses use various correlation scales in both the horizontal

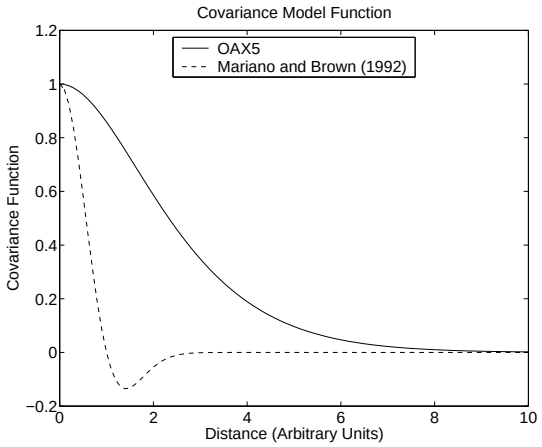

Figure 10: Covariance model weighting function applied to observations for the objective analyses. For comparison, the covariance model used in the objective analysis procedure of Mariano and Brown (1992) is also indicated, assuming unit scales.

and vertical spatial dimensions, as well as in time. Since in general more observations are available closer

to the surface (due mostly to weaker RF signals at greater depth as the aircraft proceeds downrange), smaller spatial correlation scales are used within the OML to achieve higher spatial resolution. The OAX5 optimal interpolation algorithm also yields estimates of the uncertainty of each of the gridded values, based upon the input noise estimate. This information will be used as part of an overall error analysis in the derived quantities.

The basic grid structure used for all analyses is 31×31 nodes in the horizontal dimensions encompassing a $3^\circ \times 3^\circ$ domain in latitude and longitude. The vertical grid contains 151 points every 5 m depth from the surface to 750 m. The grid is rotated 292° from true north to align with the direction of storm travel. The storm track is aligned with the 5th grid column from the left side of the domain, and the peak surface wind travels along approximately the 8th column.

Each analysis uses a 10-day temporal correlation scale, which corresponds to an e-folding time of approximately 2.9 days. Both the horizontal and vertical spatial correlation scales are varied in depth. The scales are chosen by trial-and-error to yield analyses that qualitatively best represent the data. Table 5 summarizes the vertical structuring of scales:

Depth range (m)	*Horiz. Scale (deg.)*	*Vert. Scale (m)*
0-50	0.5	20
50-100	1.5	40
100-150	2.0	60
150-200	2.5	80
200-400	3.0	100
400-600	4.0	150
600-750	5.0	200

Table 5: Horizontal and vertical correlation scales used in the objective analyses.

1) PRE-STORM

Figures 11 through 16 show objective analyses of temperature, salinity, and density for the pre-storm observations. Profiles measured during the series of research flights from 18 to 23 Sept. are used as input. Analyses are generated for year day 267.0, which corresponds to 24 Sept. at 00 UTC, therefore observations obtained later in the period (and closer in time to storm passage) are weighted more heavily. For each of the analyzed variables, horizontal planes are shown at the surface, 100, 200, and 300 m depth. Also, a series of vertical cross sections are shown at 3 locations within the observation region.

Pre-storm temperature analyses clearly identify the location of the northern extension of the Caribbean waters into the southern Gulf of Mexico. This warm core is separated from the Gulf Common Water (GCW) by the Loop Current (LC) system. The LC has been identified as a source of warm core anticyclonic rings that periodically separate and propagate westward in the Gulf of Mexico (Elliot 1982). The heat transported by these features represent an elevated source of thermal energy which Shay et al. (2000) hypothesized to be one mechanism responsible for the rapid intensification of Hurricane Opal (1995).

An additional observation is the existence of a weak cold trough running roughly parallel to the bathymetry contours on the western side of the analysis region. Hurricane Isidore passed to the south of the region on 22 Sept. (traveling west at latitude 22° N), and likely contributed to upwelling of cold water along the continental shelf. Also persistent trade winds tend to keep the thermocline near the surface off-shelf through Ekman transport. This upwelling is evident in the along-track cross section shown in Figure 12. It may also be noted that not only does the warm core contain a deeper OML than the GCW, but also that the thermocline stratification below the OML is weaker.

The salinity analyses (Figures 13 and 14) also help to resolve the distinct differences in the water masses present in the observation region. While the surface salinity shows relatively little variability, the subsurface plots indicate the deeper, more saline water that is representative of the Caribbean waters. The

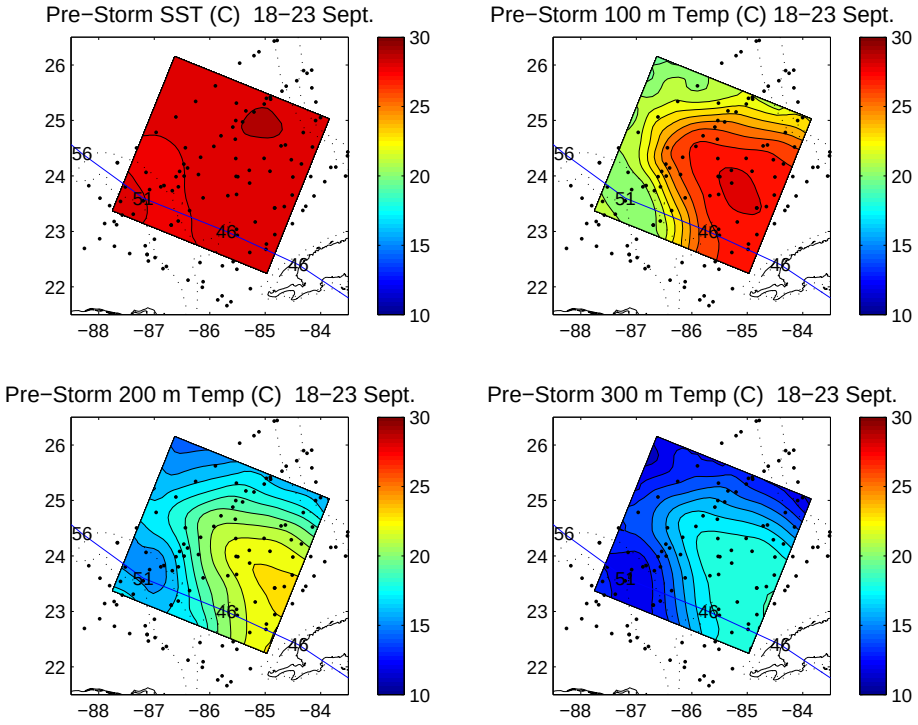

Figure 11: Pre-storm temperature on 18-23 Sept. at surface, 100, 200, and 300 m depth objectively analyzed from observed profiles. Dots indicate profile locations.

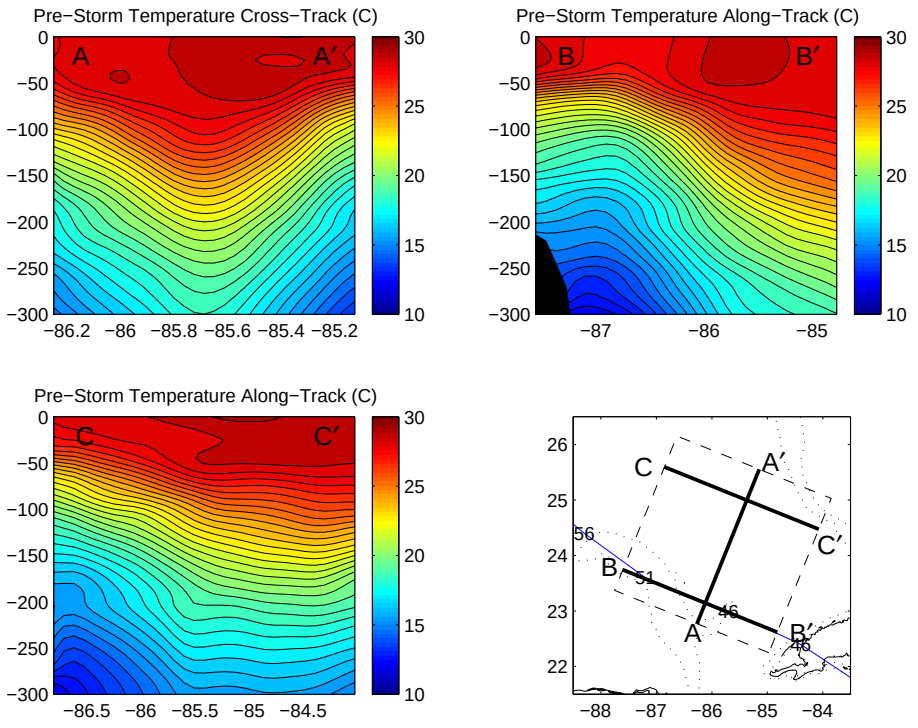

Figure 12: Pre-storm temperature vertical cross sections on 18-23 Sept. Cross-section locations are identified on the lower-right map panel.

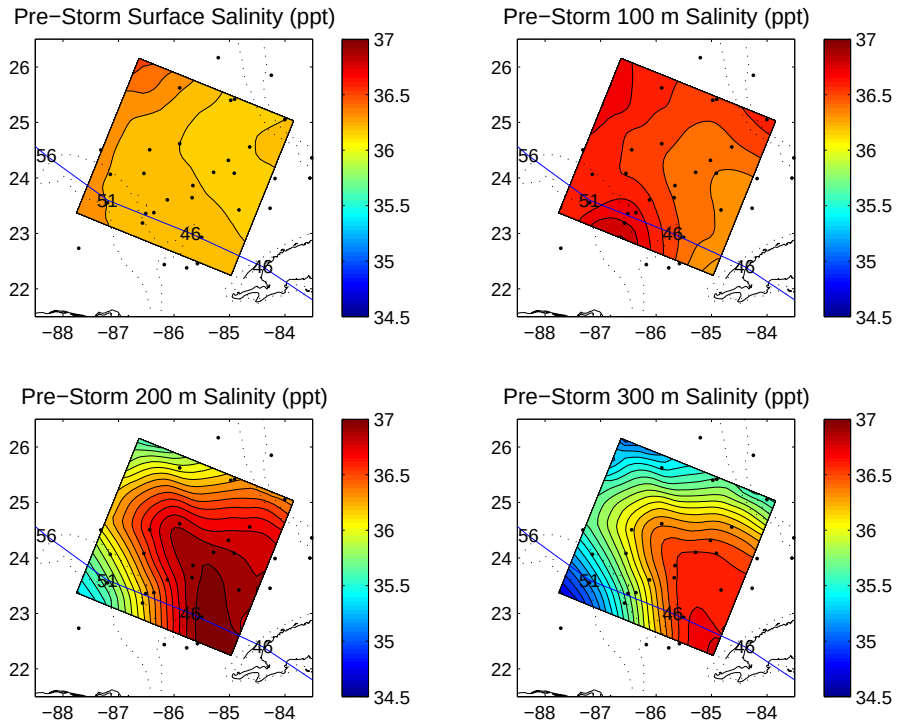

Figure 13: Pre-storm salinity on 19-23 Sept. at surface, 100, 200, and 300 m depth objectively analyzed from observed profiles. Dots indicate profile locations.

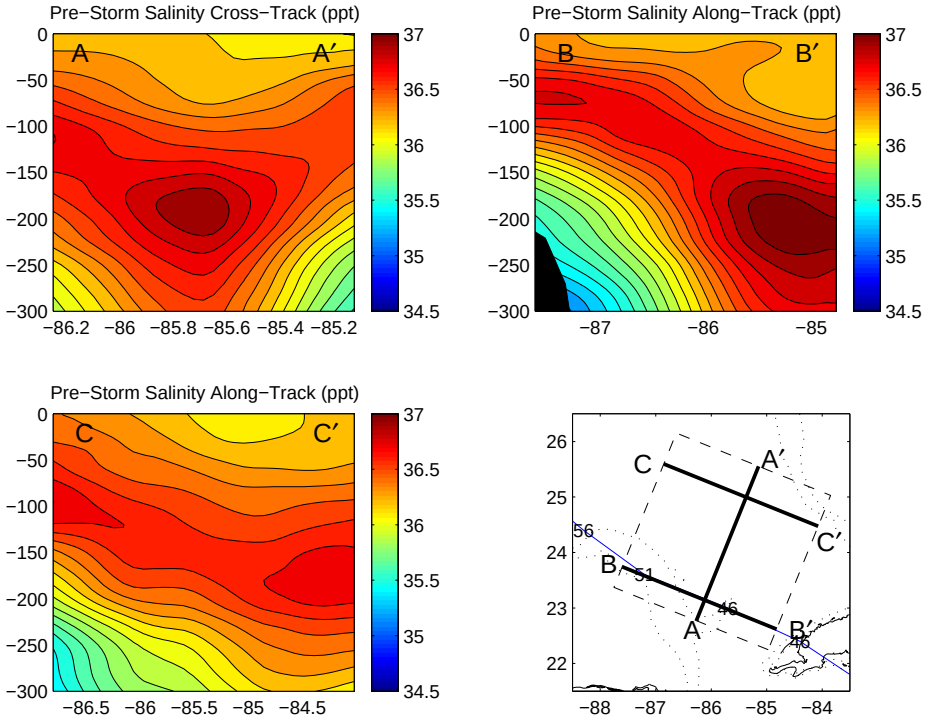

Figure 14: Pre-storm salinity vertical cross sections on 19-23 Sept. Cross-section locations are identified on the lower-right map panel.

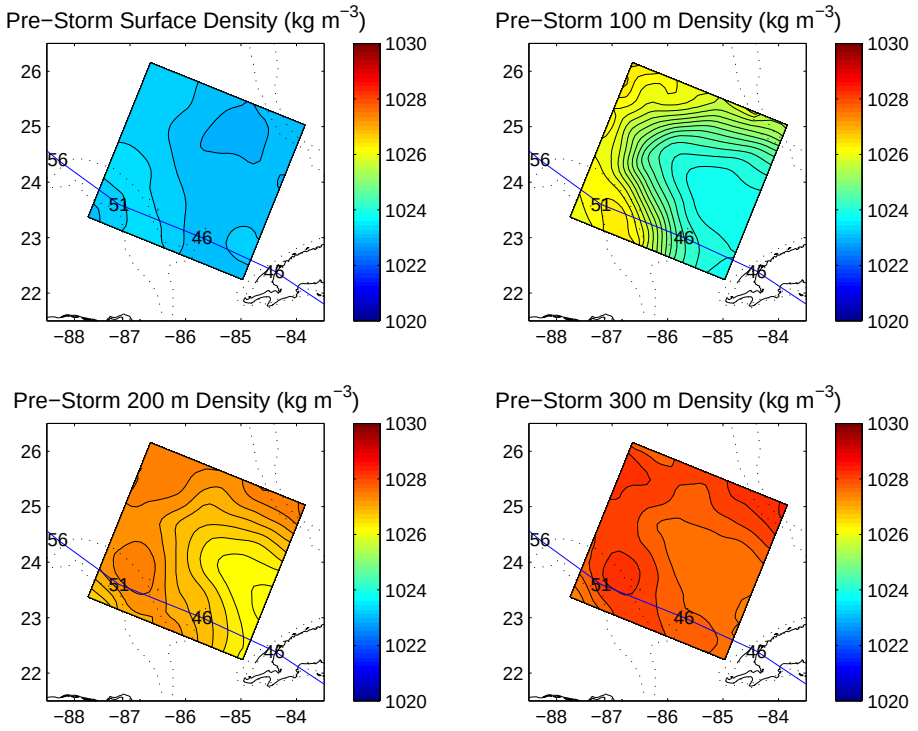

Figure 15: Pre-storm density on 18-23 Sept. at surface, 100, 200, and 300 m depth computed from objectively analyzed temperature and salinity profiles.

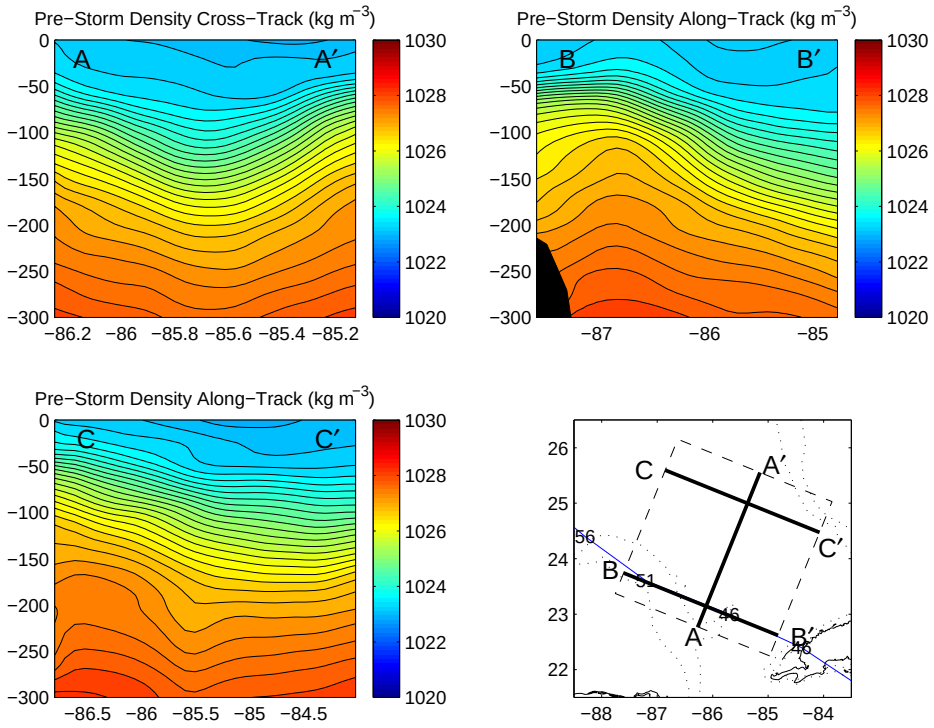

Figure 16: Pre-storm density vertical cross sections on 18-23 Sept. computed from objectively analyzed temperature and salinity observations. Cross-section locations are identified on the lower-right map panel.

warm side of the LC shows maximum salinities of nearly 37 ppt at ∼200 m depth, which contrasts with maximum values in the GCW of around 36.6 ppt at 75 m.

The mass density analyses shown in Figures 15 and 16 are computed from analyzed temperature and salinity grids. Knowledge of the distribution of mass within and below the OML is of primary importance for this research. Again, the warm core of the LC system is clearly identified. A result of the density analyses is that the strongest portion of the LC baroclinc zone exists at between roughly 50 and 150 m depth. Although a strong horizontal temperature gradient exists at greater depths, the high salinity on the warm side of the LC compensates to homogenize the density field at depths below 200 m.

2) IN-STORM

As shown in Figures 17 through 22, analyses represent the observed conditions under direct forcing from Hurricane Lili on 02 Oct. There is a comparative lack of data relative to the more intensely observed pre- and post-storm targets, as the primary focus on this flight was to measure surface atmospheric conditions responsible for the energy fluxes. A fairly complete set of SST observations were made, and the sub-surface observations will be used to evaluate the data quality observed before and after storm passage. Each of the analyses shown are identical in location to those presented in the previous pre-storm analysis section. Generally, the thermodynamic structure observed prior to storm passage persists in the in-storm data. The salinity observations are particularly weak in their coverage, and accordingly the statistical errors are expected to be large in the analyses.

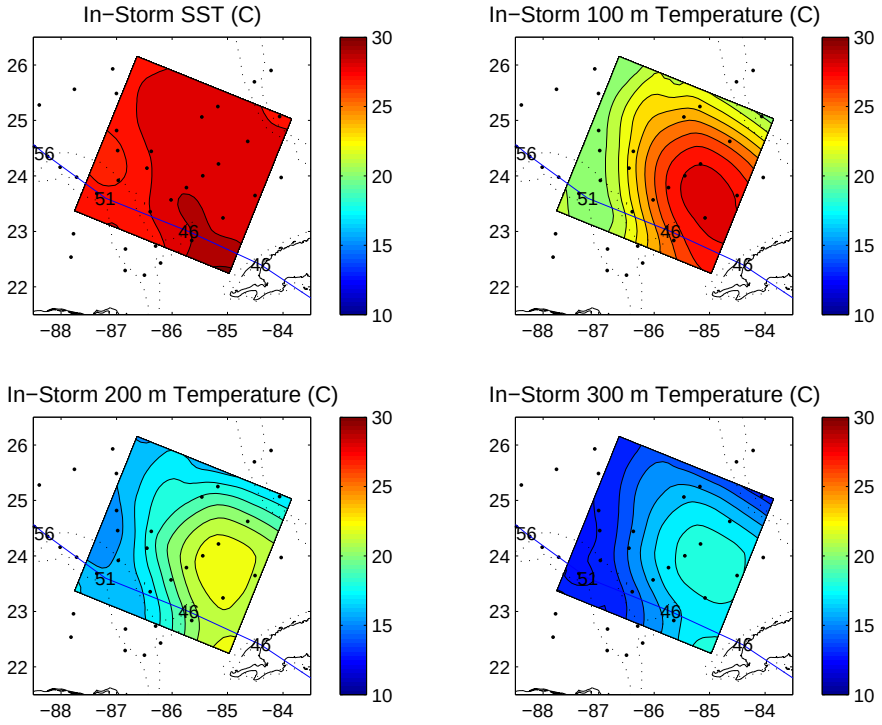

Figure 17: In-storm temperature on 02 Oct. at surface, 100, 200, and 300 m depth objectively analyzed from observed profiles. Dots indicate profile locations.

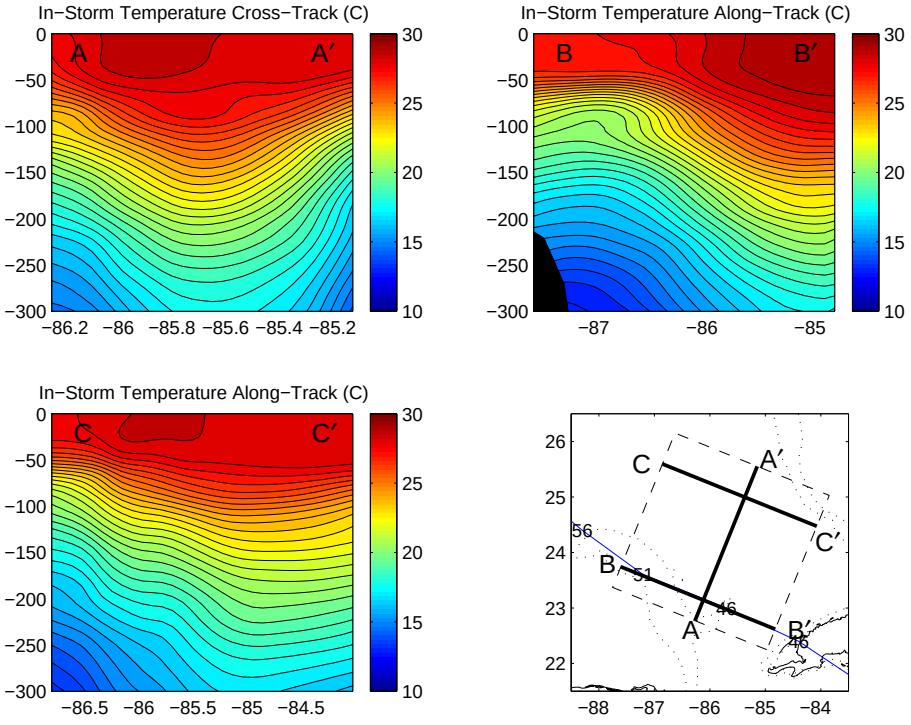

Figure 18: In-storm temperature vertical cross sections on 02 Oct. Cross-section locations are identified on the lower-right map panel.

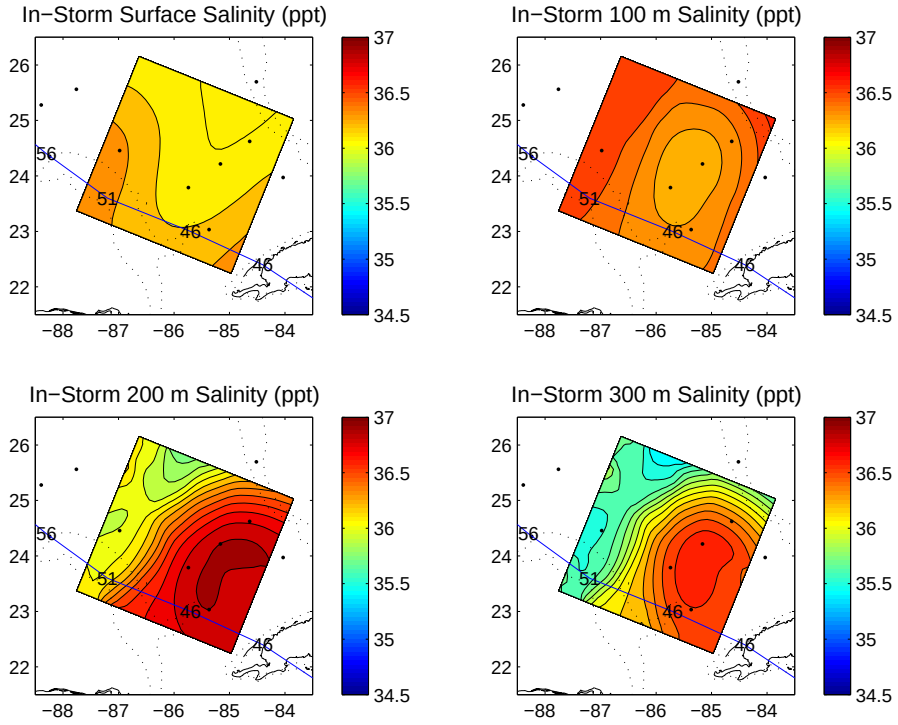

Figure 19: In-storm salinity on 02 Oct. at surface, 100, 200, and 300 m depth objectively analyzed from observed profiles. Dots indicate profile locations.

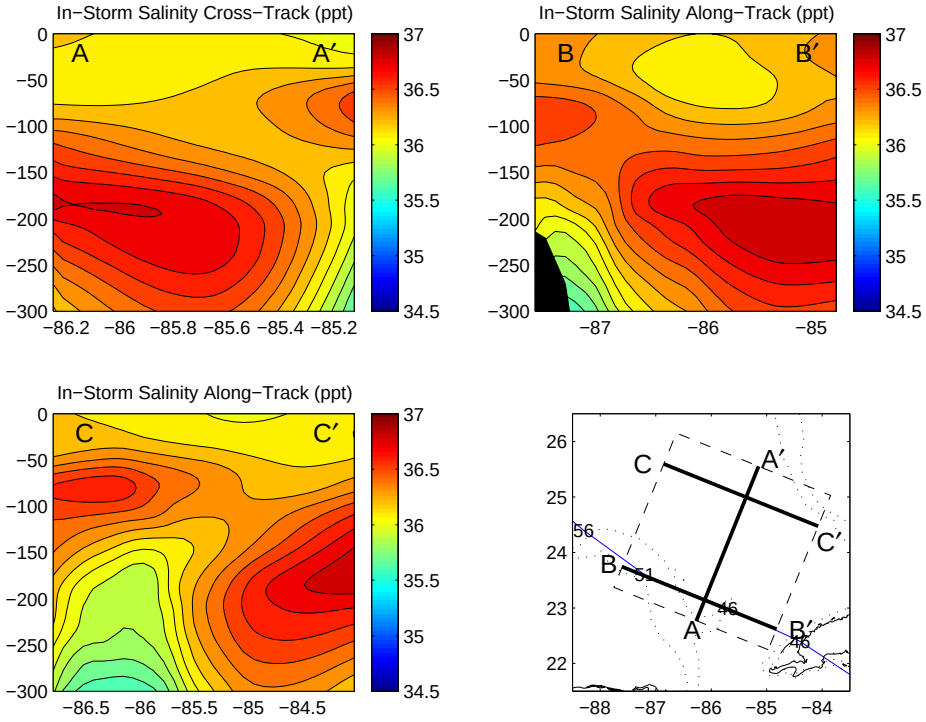

Figure 20: In-storm salinity vertical cross sections on 02 Oct. Cross-section locations are identified on the lower-right map panel.

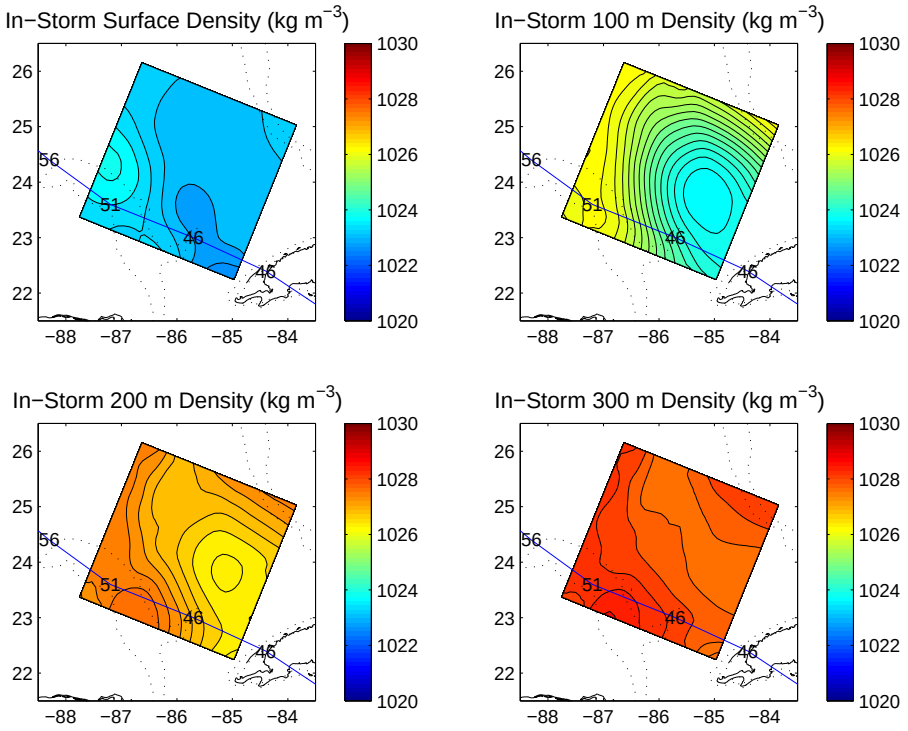

Figure 21: In-storm density on 02 Oct. at surface, 100, 200, and 300 m depth computed from objectively analyzed temperature and salinity profiles.

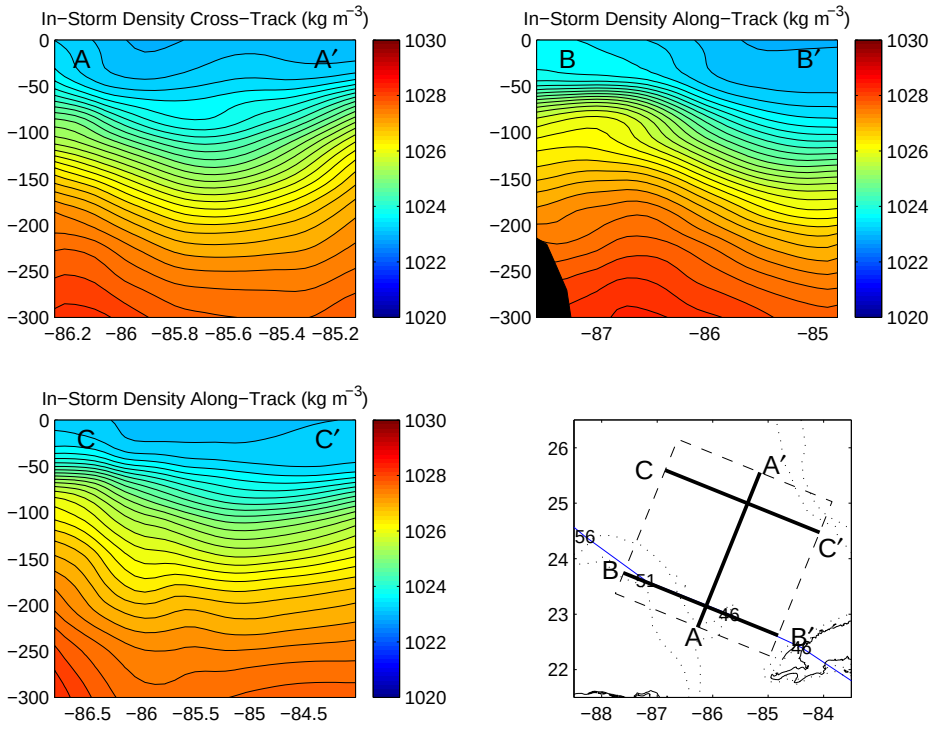

Figure 22: In-storm density vertical cross sections on 02 Oct. computed from objectively analyzed temperature and salinity observations. Cross-section locations are identified on the lower-right map panel.

3) POST-STORM

Post-storm analyses, shown in Figures 23 through 28, are produced from observations made on 04 Oct., roughly 60 hrs (2 IP) after the passage of Lili. As before, the analyses are in the same geographic location. Examining the temperature analyses, the major large-scale difference between pre-and post-storm data is in the LC itself, as its axis appears to have shifted slightly downstream. Preliminary analyses of the current data indicate a similar change in structure, which signifies a geostrophically-balanced phenomenon. Since currents generated by TCs are observed to be primarily near-inertial in nature (Shay et al. 1992), this structural change is not likely to have been induced by Lili. Additionally, it may be seen that there is relatively little evidence of surface cooling, especially in the warm core. The post-storm cooling typically observed does however begin to appear in the GCW to the right of the storm track.

d. OML quantities

Since it is of basic interest for this effort to examine the mean OML response to a TC's forcing, the quantities which describe the OML's structure are now presented. First, it is necessary to establish a clear definition of the OML. Kara et al. (2000) indicate that the depth at which the temperature decreases 0.8° C from the SST best represents the depth of turbulence penetration into the thermocline. This criterion will be applied to the objectively analyzed temperature data to estimate the OML depth. Second, the average density over this layer is computed. Figures 29 and 30 show the estimated OML depth and the average density computed over the layer. Evident in the post-storm density analysis is the slight increase to the right of the storm track due to the storm-induced cooling on the cold side of the Loop Current.

The stratification within the thermocline has been shown to be important in regulating the rate of deepening of the OML, and ultimately is proportional to the change in gravitational potential energy.

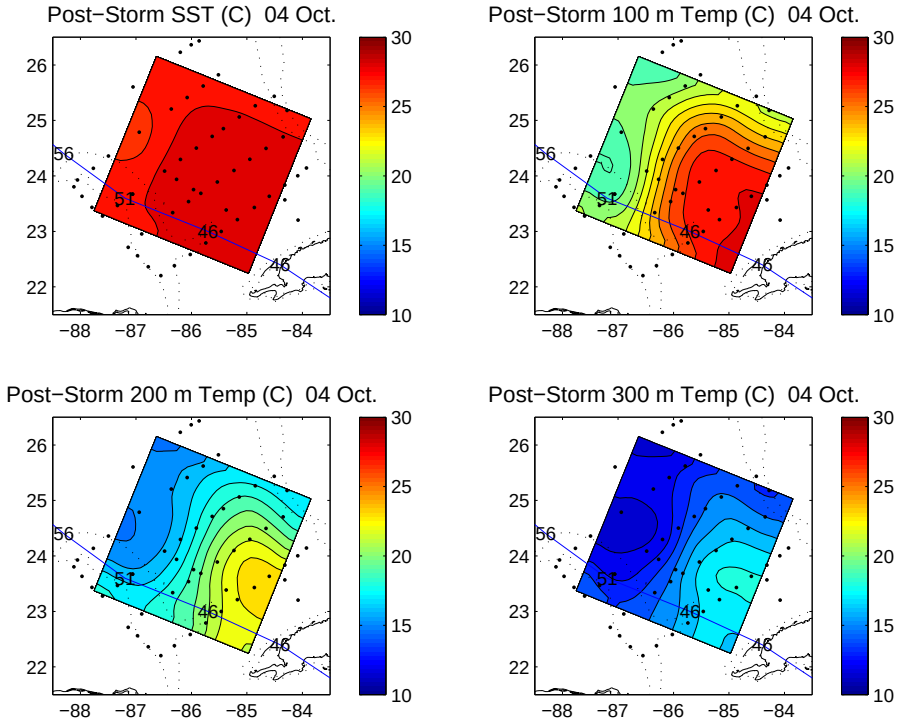

Figure 23: Post-storm temperature on 04 Oct. at surface, 100, 200, and 300 m depth objectively analyzed from observed profiles. Dots indicate profile locations.

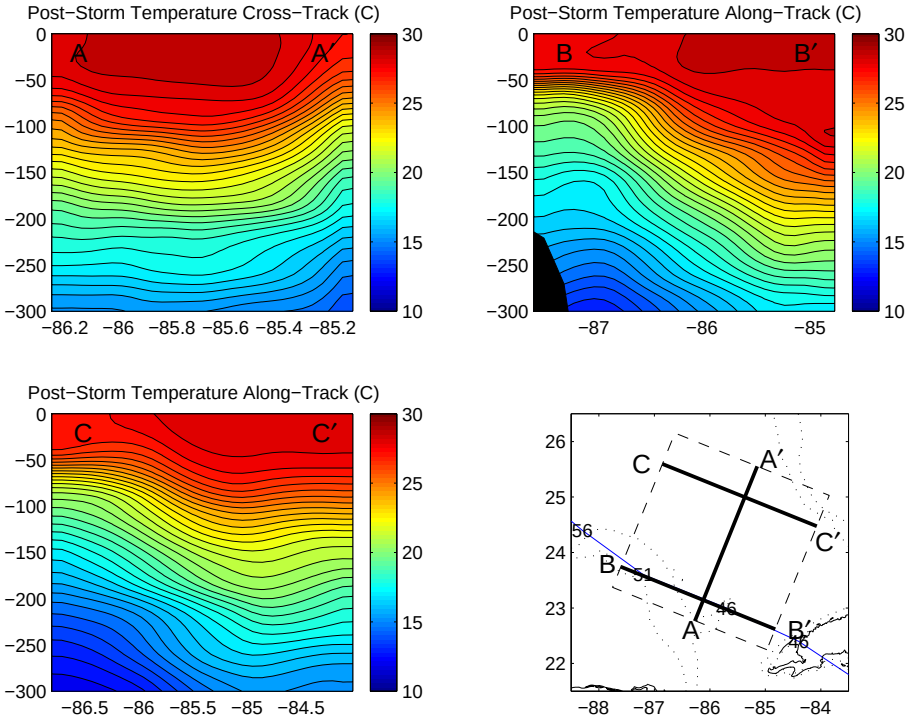

Figure 24: Post-storm temperature vertical cross sections on 04 Oct. Cross-section locations are identified on the lower-right map panel.

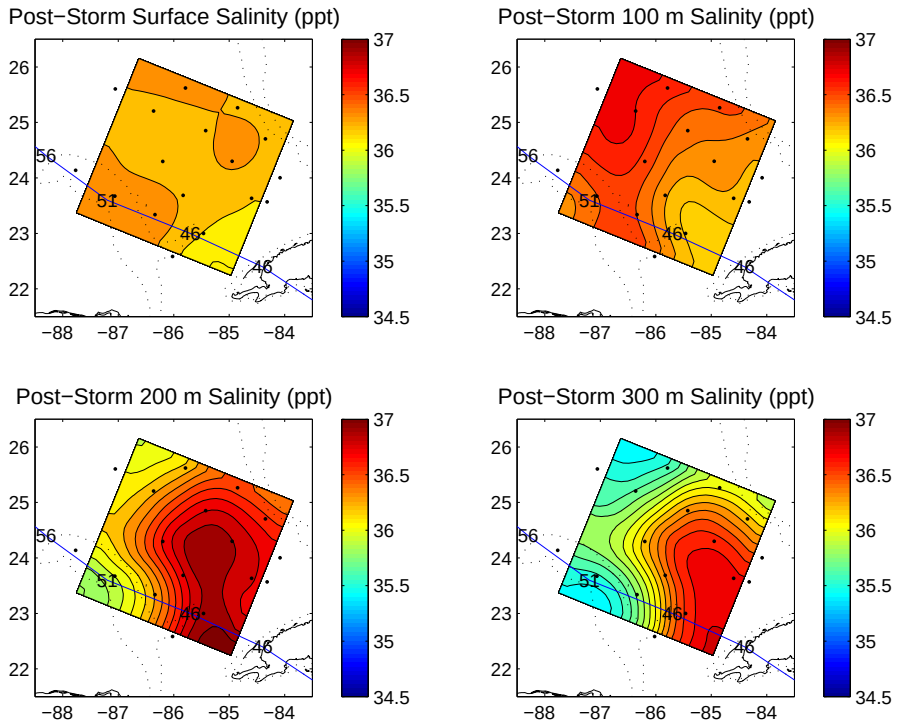

Figure 25: Post-storm salinity on 04 Oct. at surface, 100, 200, and 300 m depth objectively analyzed from observed profiles. Dots indicate profile locations.

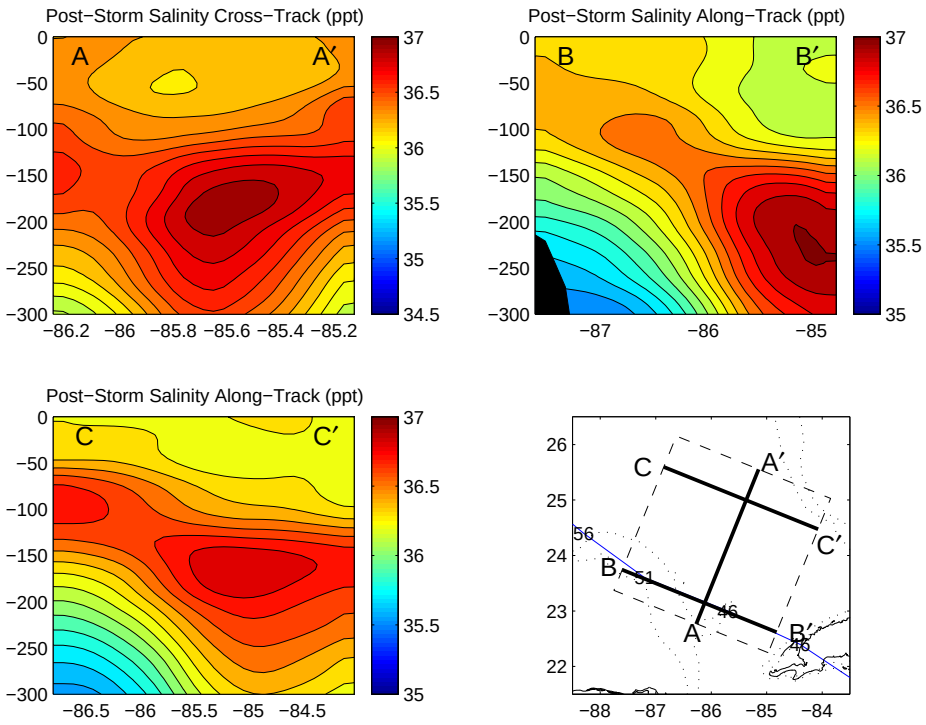

Figure 26: Post-storm salinity vertical cross sections on 04 Oct. Cross-section locations are identified on the lower-right map panel.

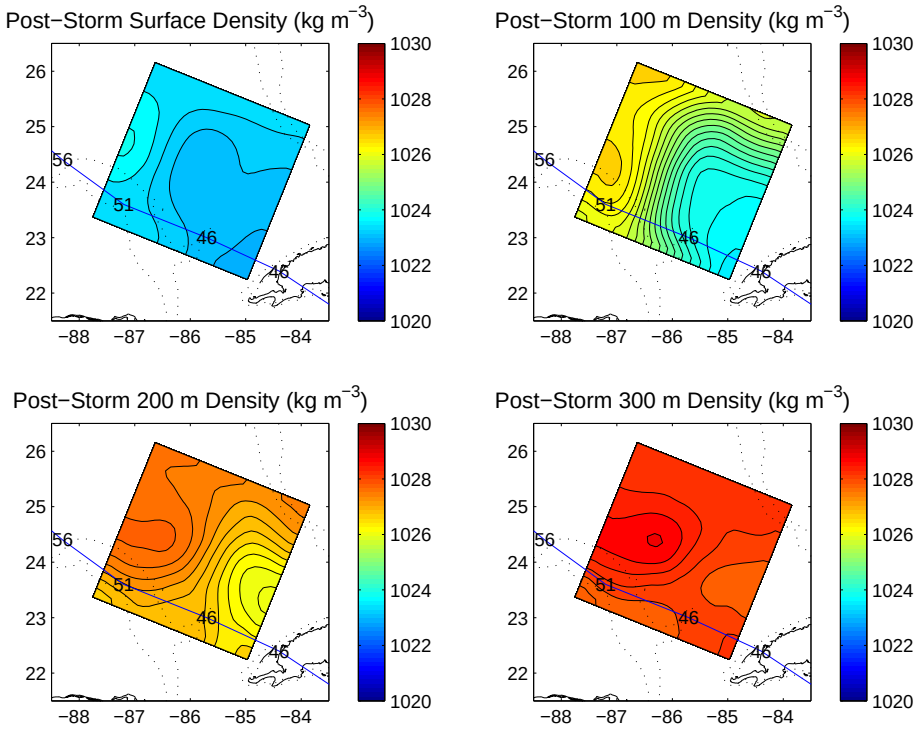

Figure 27: Post-storm density on 04 Oct. at surface, 100, 200, and 300 m depth computed from objectively analyzed temperature and salinity profiles.

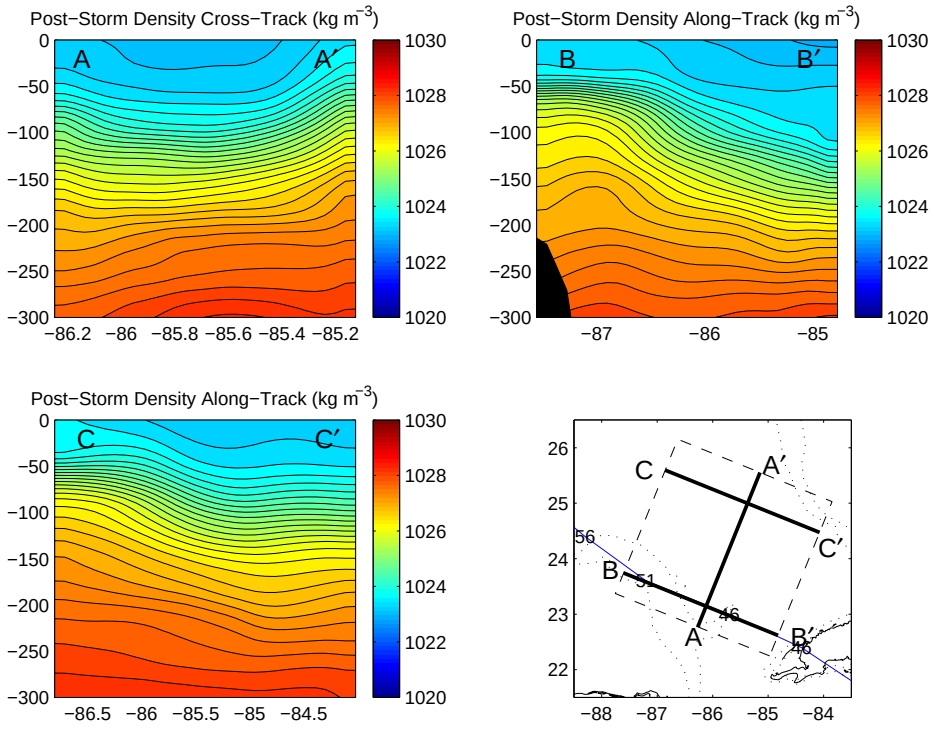

Figure 28: Post-storm density vertical cross sections on 04 Oct. computed from objectively analyzed temperature and salinity observations. Cross-section locations are identified on the lower-right map panel.

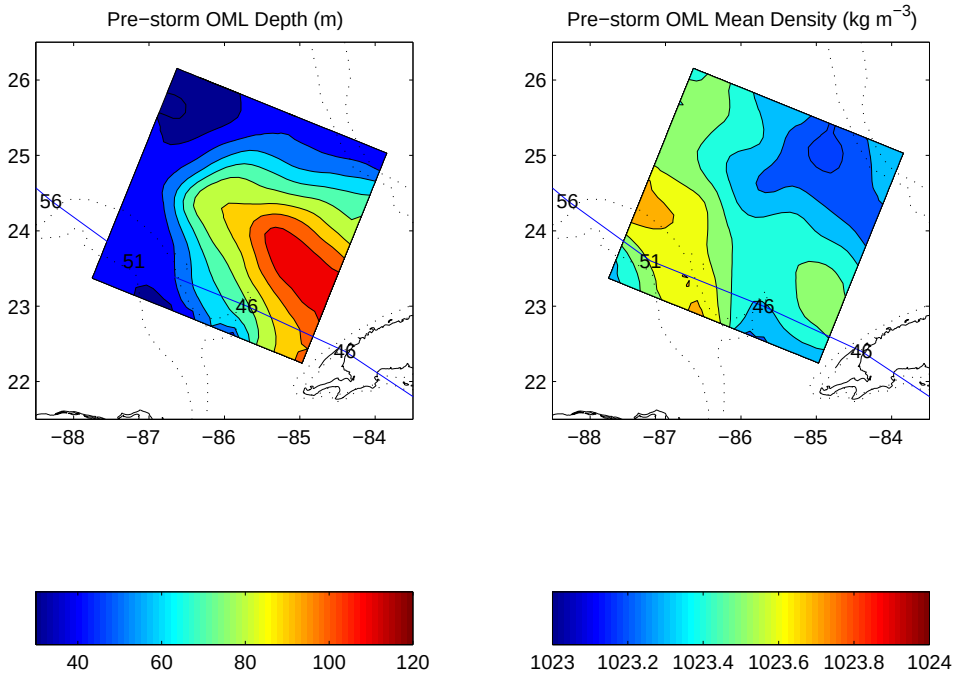

Figure 29: OML depth (left panel), and vertically-averaged density in OML for pre-storm analysis.

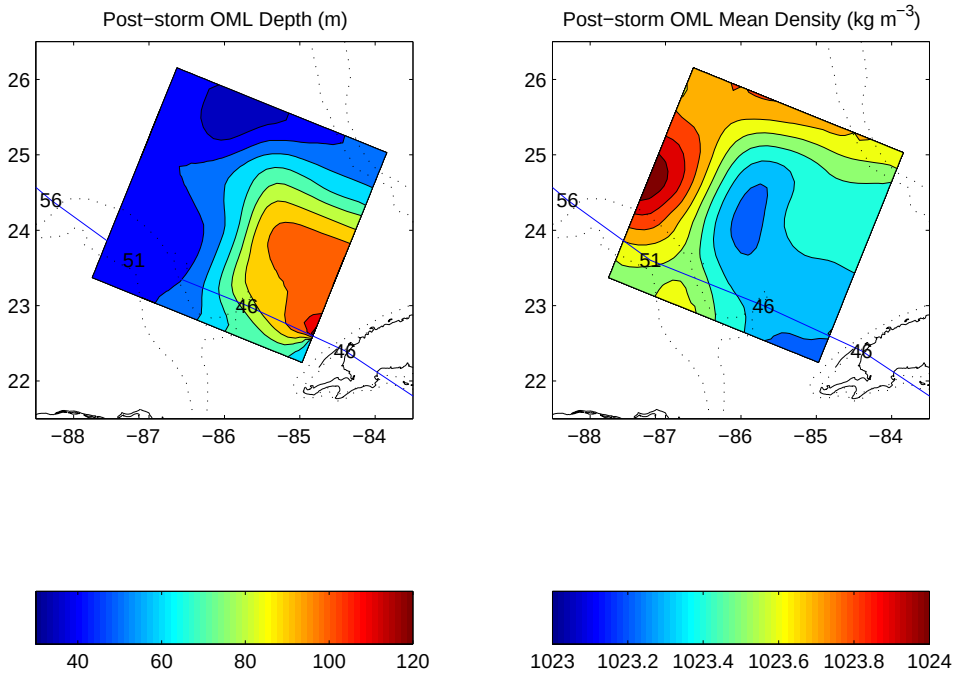

Figure 30: Same as Fig. 29 but for post-storm.

Figures 31 and 32 show estimates of the horizontal distribution of stratification below the base of the OML. The density perturbation (ρ') is calculated as the change in density over layer of thickness chosen to be 50 m. Correspondingly, the stratification frequency (N) is shown in adjacent panels, where:

$$N = \sqrt{\frac{g}{\rho_0}\frac{\rho'}{\Delta z}}. \tag{45}$$

e. Current analysis

Most attention to this point has been given to the analysis of the observed thermodynamic conditions. Preliminary efforts have involved post-processing of AXCP current profiles and removal of surface wave induced orbital velocities. Aside from estimating the OML current generated by storm passage, it was an experimental goal to observe the pre-existing mesoscale current field, which might be responsible for significant advective tendencies in the overall upper-ocean energy budget. By far the most striking feature observed here is the strong baroclinic zone separating the Caribbean warm core extension from the GCW, and its associated rapid LC system.

The current profiles measured by AXCPs contain estimates of the total flow field, which consists of the horizontal current (mean plus turbulent), in addition to local orbital velocities due to surface wave propagation. To estimate the mean OML current field, and therefore the mean KE as part of the larger OML mechanical energy budget, it is important to remove the surface wave induced orbital velocity signal from the current profile, since when averaged over a cycle, the waves will not contribute significantly to the mean current (with the exception of a small Stokes drift due to non-linear wave structure). The procedure detailed in (Sanford et al. 1987) to indentify the wave-induced signal has been applied successfully to a number of cases including current profiles in tropical cyclones (Shay et al. 1992). The observed current is

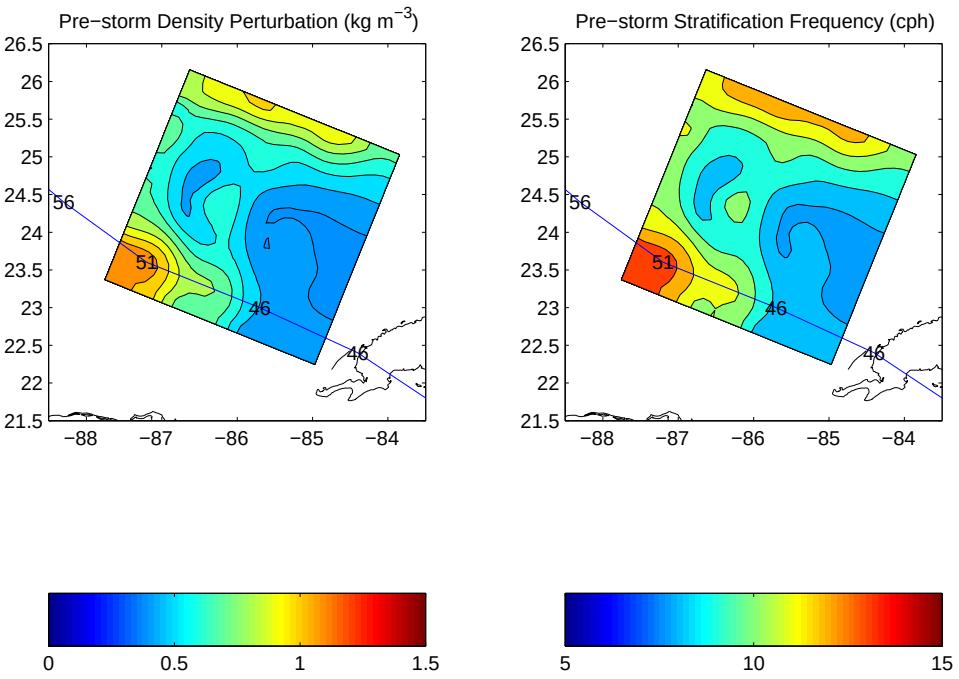

Figure 31: Thermocline density perturbation (left panel) and corresponding stratification frequency (cycles per hour, right panel) for pre-storm analysis.

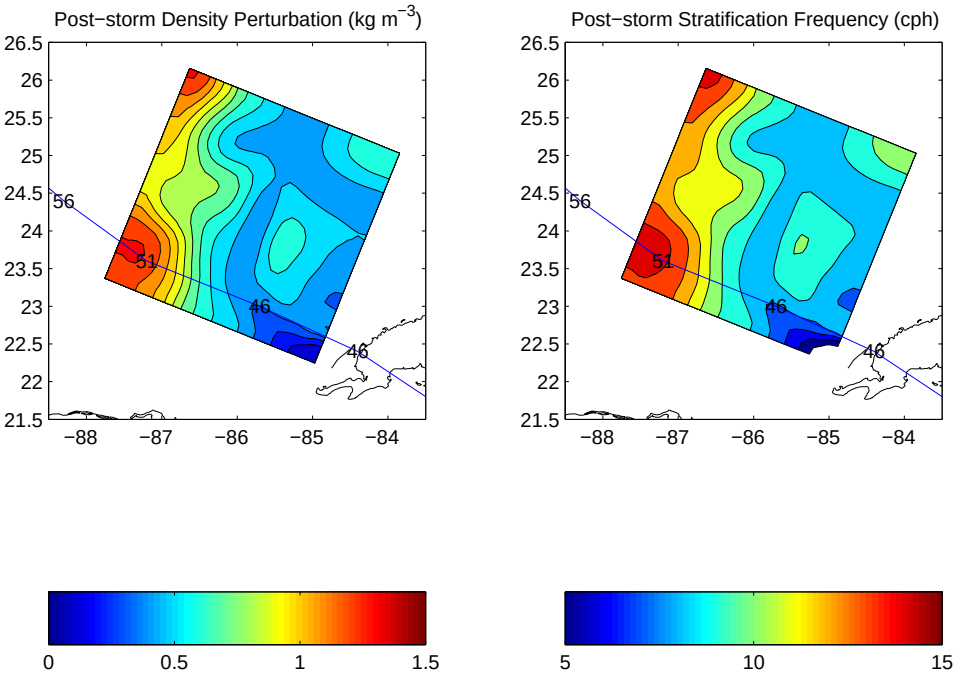

Figure 32: Same as Fig. 31 but for post-storm.

fit to a three-layer model with a monochromatic linear deep water surface gravity wave superimposed:

$$\begin{aligned} u(z) &= \left[C\cos\left(\frac{\omega z}{W}\right) + S\sin\left(\frac{\omega z}{W}\right)\right] e^{kz} \\ &+ U_i + U_{z_i}\left[z - \left(\frac{z_{i-1} - z_i}{2}\right)\right] \quad (i = 1, 3), \end{aligned} \tag{46}$$

where $u(z)$ is the modeled east-west current profile (a similar expression holds for the north-south component), $\omega = \sqrt{kg}$ is the wave frequency for wavenumber k, $W = -4.5\,\mathrm{m\,s^{-1}}$ is the AXCP fall rate, and U_i and U_{z_i} are the mean current and shear in layer i, respectively. The observed current profile is fit to Equation 46 using a standard Levenberg-Marquardt nonlinear least-squares regression (Marquardt 1963) by minimizing the error over a range of trial wave periods $T = 7$ to 14 s ($\omega = 2\pi/T$). Additional constraints are applied at the interfaces between layers to ensure continuity, which reduces the number of free parameters from eight to six.

Figure 33 shows some fitted current profiles for observations obtained during the Lili in-storm mission on 02 Oct. in various regions of the storm. Residual errors in the surface wave layer ($kz > -2$) are typically around 3-5 $\mathrm{cm\,s^{-1}}$, and throughout the upper 200 m depth are generally 5-10 $\mathrm{cm\,s^{-1}}$.

The observed mean OML currents (U_1, V_1) determined from the profile fits are objectively analyzed for pre- and post-storm data in Figures 34 and 35, respectively. The LC is clearly revealed in the analyses, and shows peak pre-storm OML current speeds of $\sim$1.2 $\mathrm{m\,s^{-1}}$. Interestingly, the post-storm analysis indicates slightly *weaker* currents to the right of the storm track in core of the LC jet.

Finally, a preliminary assessment of the storm-induced shear at the base of the OML is made. The current profile fitting method estimates the slope (shear) in a layer below the OML (U_{z_2}, V_{z_2}). The shear vector is objectively analyzed and the the shear "production" term in the bulk Richardson number is

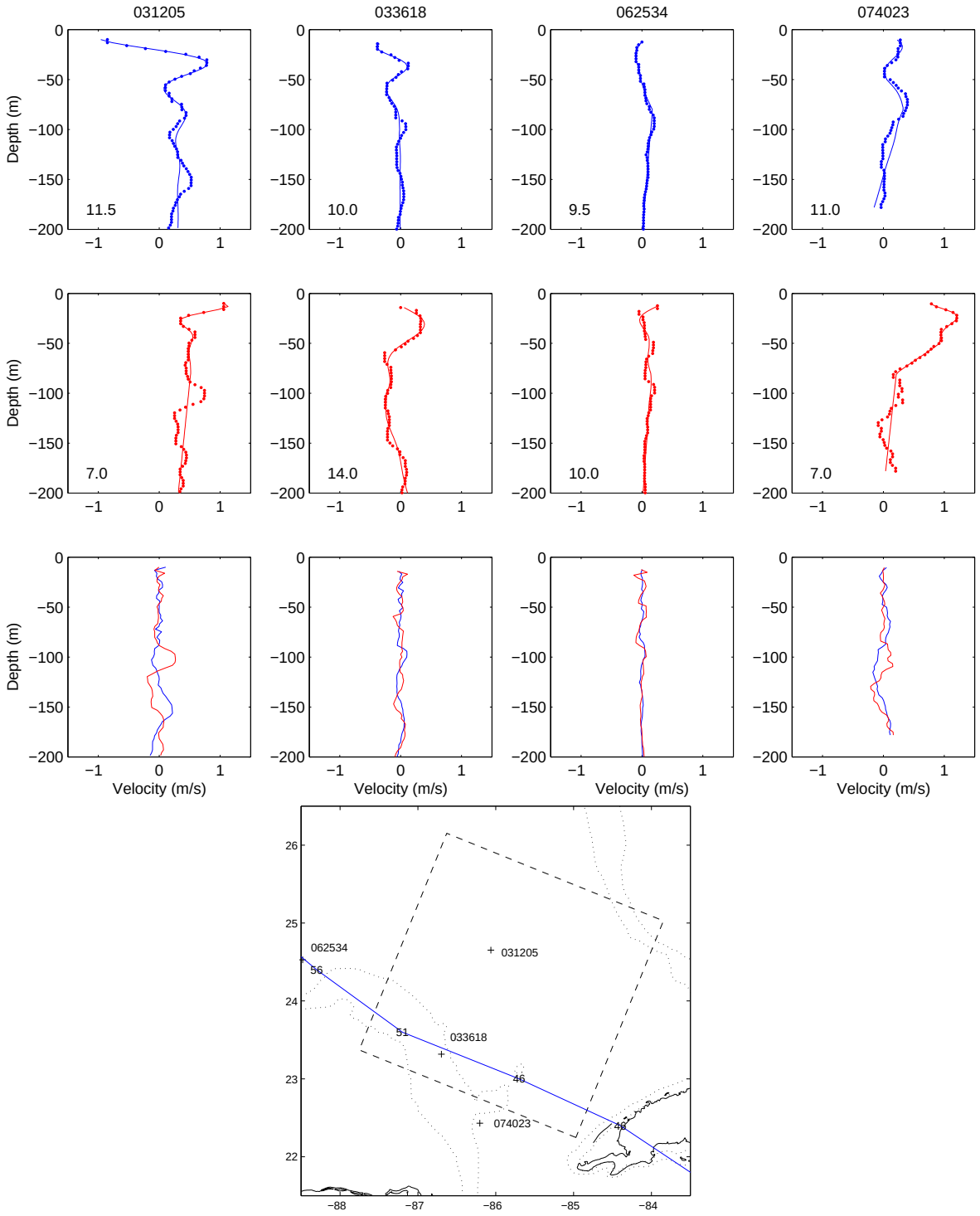

Figure 33: Observed (dots) and fitted (solid lines) current profiles observed by AXCP on 02 Oct (in-storm). Top row is eastward component (U) and middle row is northward (V). Bottom row shows residuals for U (blue) and V (red). The locations of the profiles, identified by time at the top of columns, are shown on the map relative to the storm track. Estimated wave period (s) is indicated for each profile.

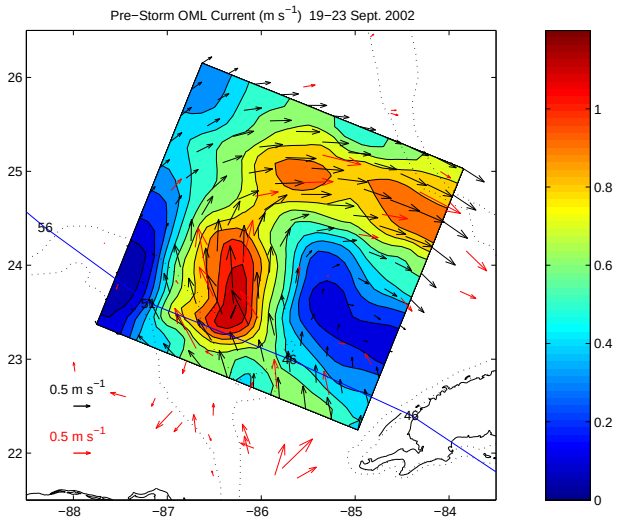

Figure 34: Observed (red vectors) and analyzed (black) mean OML currents based on fitted current profiles from pre-storm flights on 19-23 Sept. The profiles obtained in H. Isidore on 21 Sept. (at $\sim 22\circ$ N) were not used in the objective analysis.

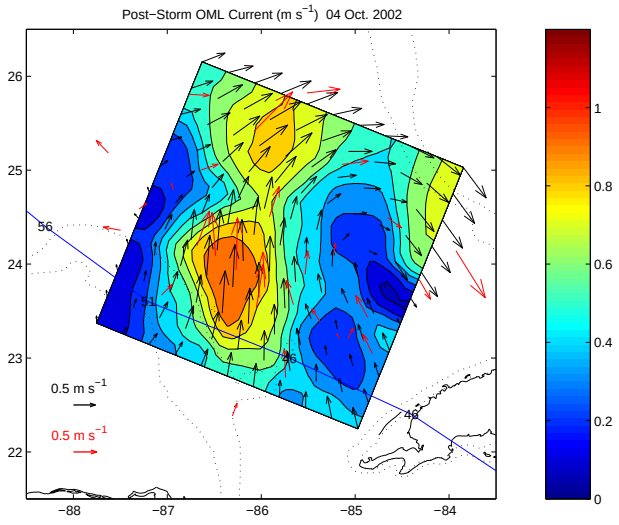

Figure 35: Same as Fig. 34 but for post-storm.

computed by:

$$S^2 = \left[(U_{z_2})^2 + (V_{z_2})^2\right] . \tag{47}$$

Figure 36 shows the pre-storm and Figure 37 the post-storm shear estimates. The pre-storm shear vector field shows weak coherence, and the strong shear to the south of the analysis is associated with measurements made in Hurricane Isidore. In contrast, the post-storm analysis identifies the effect of Lili, with enhanced current shears as the storm exists the LC to the northwest.

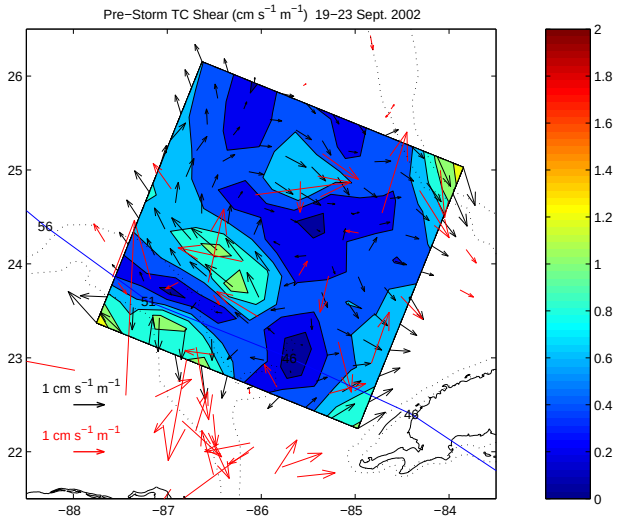

Figure 36: Shear production S^2 computed from Equation 47 for pre-storm current profiles. Also plotted are the analyzed (black) and observed shear vectors (red). As for the current analyses, shear estimates obtained in H. Isidore on 21 Sept. are not used in the objective analysis.

f. Air-sea parameters and scaling

To provide an initial comparison of conditions observed here with those from previous studies (Price 1981; Shay et al. 1989, 1990, 1992), a number of parameters and non-dimensional numbers which are known to govern the upper-ocean response are estimated. Previous studies have generally involved developing a set of parameters that describe the initial horizontal upper ocean mean structure. This study differs in some respects, however, since significant variability was observed across the LC. Mean parameters (Ta-

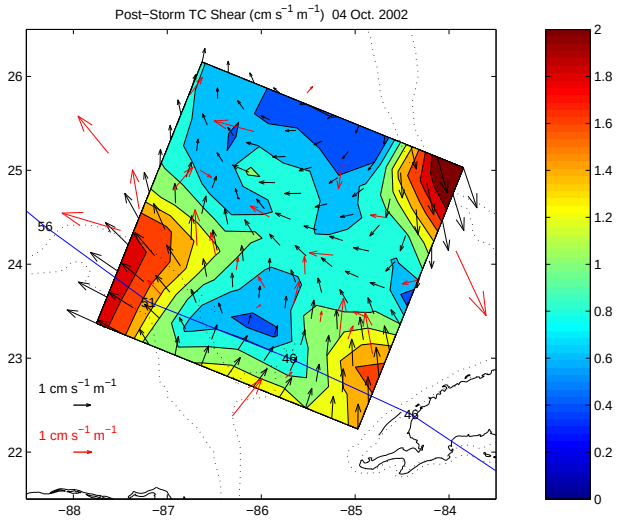

Figure 37: Same as Fig. 36 but for post-storm analysis.

ble 6) and scales (Tables 7 and 8) are computed, along with a range of variability over the observational domain. For comparison purposes, results from previous studies of ocean response are restated here.

Parameter	*This study*	*S89*	*S90*	*S92*	*P83*
OML depth H (m)	65 (35-110)	30	30	30	50
Thermocline scale thickness D (m)	100	160	200	200	200
Density perturbation ρ' (kg m^{-3})	1.6 (0.5-2.5)	3.1	2.3	4.1	4.0
Radius of max. stress R_{max} (km)	25	34	30	50	40
Max. stress T (N m^{-2})	6.5	4.4	3.3	3.3	2.0
Storm speed V (m s^{-1})	7.1	4.0	6.5	5.6	7.0
Inertial period $2\pi/f$ (hr)	31.2	36.0	24.0	30.0	28.3

Table 6: Independent variable scales governing the upper-ocean response. The column containing initial results for this study give average values over the observational domain, with minima and maxima in parentheses. For comparison the values reported in the observational studies of Shay et al. (1989), Shay et al. (1990), and Shay et al. (1992), and the modeling work of Price (1983) are restated here, labeled as S89, S90, S92, and P83, respectively.

g. Error estimates

Inherent in the measurements of temperature, salinity and currents (and associated derived quantities) are observational uncertainties. An additional source of uncertainty arises when the measurements are carried over to the grid in the objective analysis ("mapping" errors). Jacob et al. (2000) outlines a procedure

Parameter	*This study*	*S89*	*S90*	*S92*	*P83*
Wind driven current $TR_{max}/\rho_0 HV$ ($\mathrm{m\,s^{-1}}$)	0.4 (0.1-0.7)	1.2	0.5	0.6	0.2
Kinetic energy $T^2R_{max}^2/\rho_0^2 HV^2$ ($\mathrm{m^3\,s^{-2}}$)	8.0 (4.9-14.8)	43.2	7.4	10.8	2.6
Internal wave phase speed NH ($\mathrm{m\,s^{-1}}$)	1.2 (0.7-1.5)	2.1	2.1	2.8	2.8
Geisler wavelength $2\pi V/f$ (km)	800	440	580	600	710

Table 7: Dependent variable scales governing the upper-ocean response. Column labels are as in Table 6.

Parameter	*This study*	*S89*	*S90*	*S92*	*P83*
Non-dimensional storm speed	2.5	1.2	1.4	0.9	1.4
Rossby number	0.3 (0.2-0.5)	0.7	0.2	0.2	0.1
Ekman number	4.3 (1.0-4.5)	2.5	2.9	3.0	3.2
Burger number	0.2 (<0.1-0.4)	0.4	<0.1	0.2	0.1
Froude number	0.2 (<0.1-0.2)	0.5	0.3	0.1	0.4

Table 8: Non-dimensional scales governing the upper-ocean response. Column labels are as in Table 6.

for estimating uncertainties in derived OML heat budget quantities based on assumed measurement errors. They applied the method to the example of uncertainties in the estimated surface heat flux (σ_{Q_0}):

$$\begin{aligned} \sigma_{Q_0} &= \rho_a C_k (C_p \Delta T + L_v \Delta q) \sigma_{U_{10}} \\ &\quad + \rho_a C_k U_{10} (C_p \sigma_{\Delta T} + L_v \sigma_{\Delta q}), \end{aligned} \tag{48}$$

where $\sigma_{U_{10}}$, $\sigma_{\Delta T}$, $\sigma_{\Delta q}$ are the (rms) uncertainties in the measured surface wind speed, air-sea temperature difference and air-sea humidity difference, respectively. Other variables have their usual meaning, and it has been assumed for simplicity that the exchange coefficients of sensible and latent heat are equal. This method will serve as a basis for preliminary error analysis of observations obtained as part of this research.

Further uncertainty is introduced by the objective analysis. The OAX5 optimal interpolation computes gridpoint error estimates based on input observational uncertainties. As do the estimates of interpolated mean quantities, the errors depend upon the covariance model used. It is proposed that a number of forms of the model will be tested to examine the effects on the computed error estimates. Additionally, mapping errors will be computed by directly comparing interpolated profiles with observed profiles.

5. Internal Budget Quantities

The first research objective is to estimate OML mechanical energy and vorticity budget quantities forced by Hurricane Lili. Observations of thermodynamic and current structure indicate that the storm traversed a highly complex region of the ocean, with strong horizontal temperature and salinity gradients and energetic currents. To examine ocean changes induced by the storm, it is first necessary to identify pre-existing features and to remove these quantities from the observed data. It is of interest to identify both pre-existing and storm-induced balanced geostrophic currents to isolate the storm-generated, near-inertial current response.

a. Geostrophic currents and vorticity

Pre-storm velocities in the observational domain are due primarily to the presence of the LC, and additionally to pre-existing wind-driven currents from Hurricane Isidore's passage to the south on 21 Sept. Although Isidore's core winds did not directly impact the observation region, it emerged from the Northern Yucatan peninsula with an extensive circulation of surface winds of 10-15 $\mathrm{m\,s^{-1}}$. The pre-storm (19-23 Sept.) thermodynamic analyses are used to estimate the balanced geostrophic current ($\vec{u}_g$) relative to a depth of 750 m using the following equation:

$$\vec{u}_g = -\frac{g}{f}\,\mathbf{k} \times \nabla\psi, \tag{49}$$

where ψ is the dynamic height (m), computed from the geopotential anomaly distribution (Fofonoff and Millard 1983).

Similar to the analyses of the thermodynamic fields, the pre-storm geostrophic velocity structure is shown in Figures 38. Maximum near-surface gestrophic velocities are found in the LC to be $\sim$0.8 $\mathrm{m\,s^{-1}}$,

decreasing to $\sim$0.4 $\mathrm{m\,s^{-1}}$ at 300 m depth. The importance of accurate salinity observations is notable, since assuming a simple domain-averaged salinity ($\sim$35.8 ppt) would lead to a 0.4 $\mathrm{m\,s^{-1}}$ overestimate in the near surface geostrophic current. From these analyses, the OML geostrophic current and relative

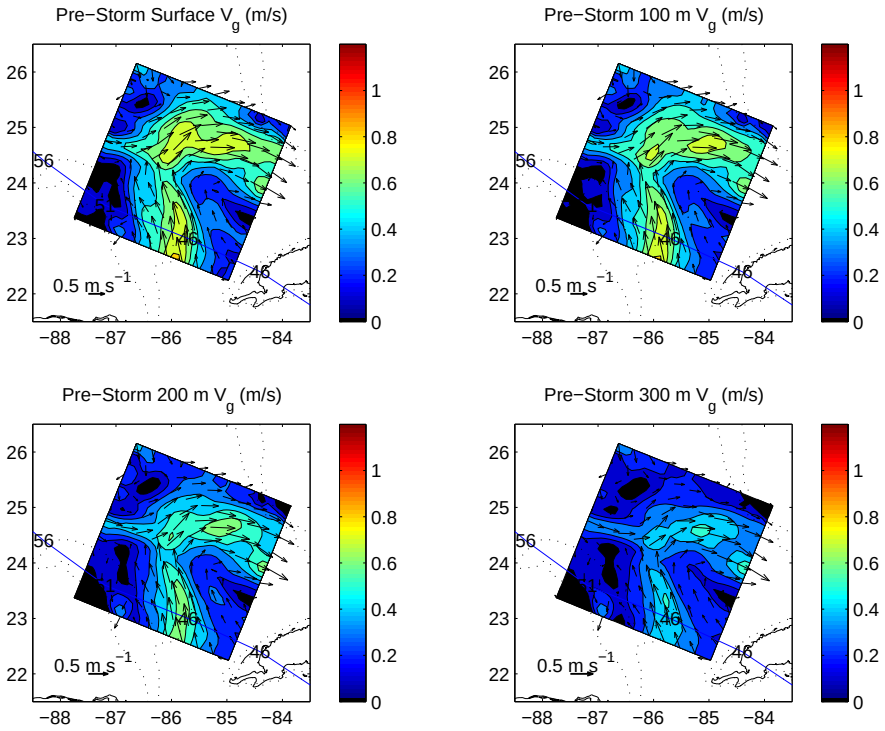

Figure 38: Pre-storm geostrophic velocity on 19-23 Sept. at surface, 100, 200 and 300 m depth computed from the observed thermodynamic fields.

vorticity fields are estimated as shown and Figure 39. The vorticity analysis indicates a peak anticyclonic rotation in the LC core of $-2.9 \times 10^{-5}\mathrm{s}^{-1}$, or about $-0.45f$.

Post-storm geostrophic currents are calculated from the density fields to help delineate the storm induced geostrophic current field, that is, the balanced current resulting from the isopycnal displacement. Shay et al. (1998) indicate storm-induced geostrophic currents of 0.1 to 0.2 $\mathrm{m\,s^{-1}}$ from Hurricane Gilbert. Figure 40 show the post-storm geostrophic current analysis and the derived geostrophic relative vorticity field. The storm-induced geostrophic currents may be estimated by computing the difference in pre- and post-storm fields. (Figure 41).

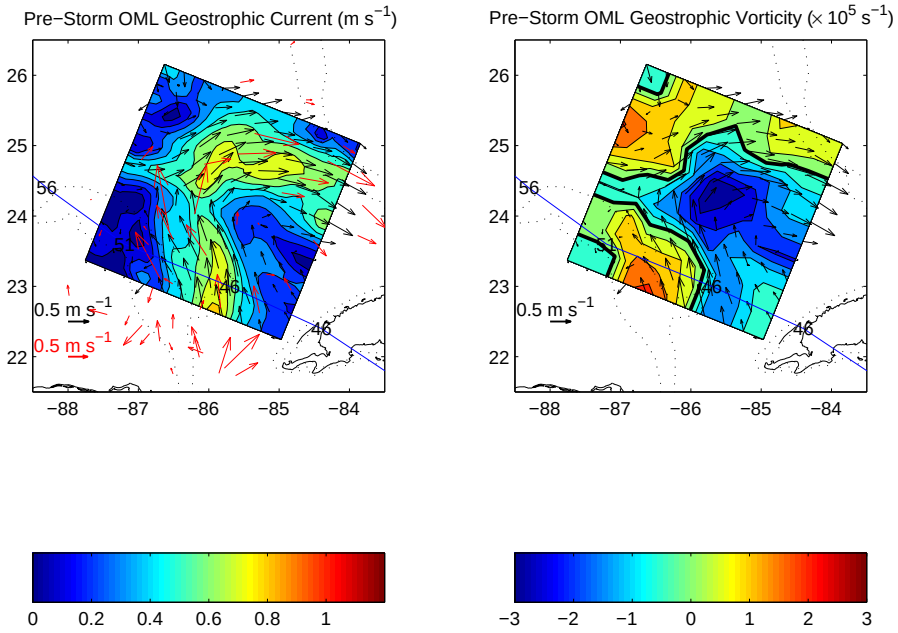

Figure 39: Pre-storm OML geostrophic current (left panel) and geostrophic relative vorticity (right panel). The observed OML currents are indicated by red vectors.

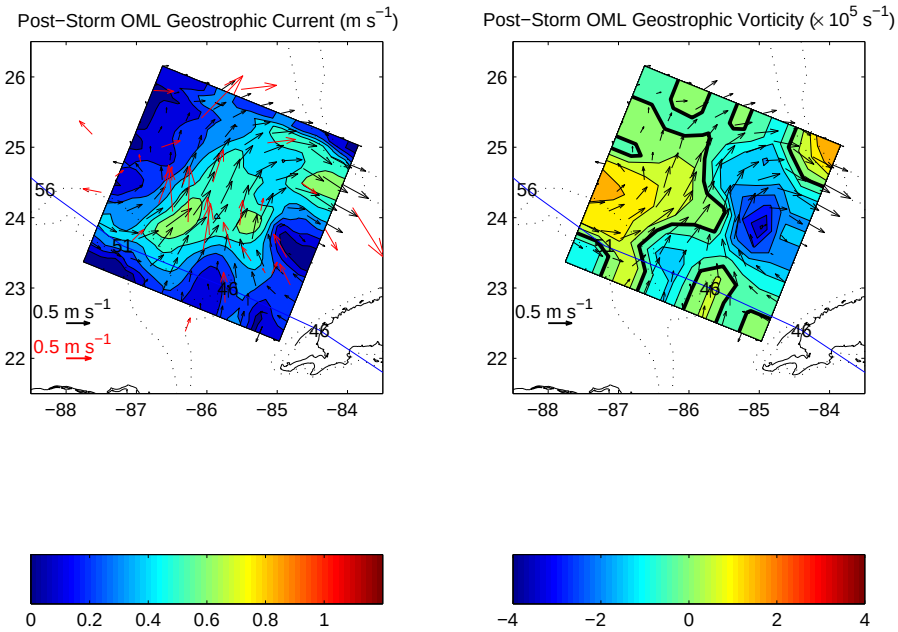

Figure 40: Same as Figure 39 but for post-storm.

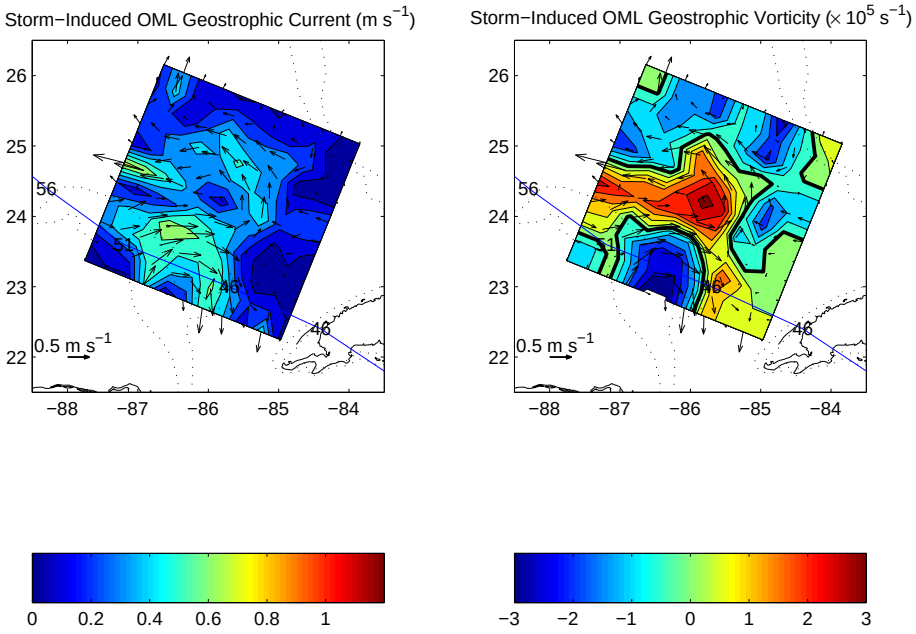

Figure 41: Storm-induced gestrophic current (left) and relative vorticity (right).

b. Near-inertial velocities

With balanced geostrophic current estimates available, the storm-induced near-inertial current response may be examined. The observed velocity (less surface wave-induced orbital velocities) is:

$$\vec{u} = \vec{u}_g + \vec{u}_i + \vec{u}_r, \tag{50}$$

where $\vec{u}_g$ is the pre-existing minus storm-induced geostrophic current, $\vec{u}_i$ is the near-inertial current, and $\vec{u}_r$ is a residual. The observed OML current has been estimated from the current profile fits (Section 4). The geostrophic current is interpolated to the profile location from the gridded field and removed from the observed current to form the vector $\vec{u}_i + \vec{u}_r$. Using the method described in Jacob et al. (2000), the profile location is transformed to a storm-relative, time/space grid using the mean storm speed V = 7.0 $\mathrm{m\,s^{-1}}$ and radius of maximum wind R_{max} = 25 km. Locations of the profiles for in-storm and post-storm profiles are shown in Figure 42.

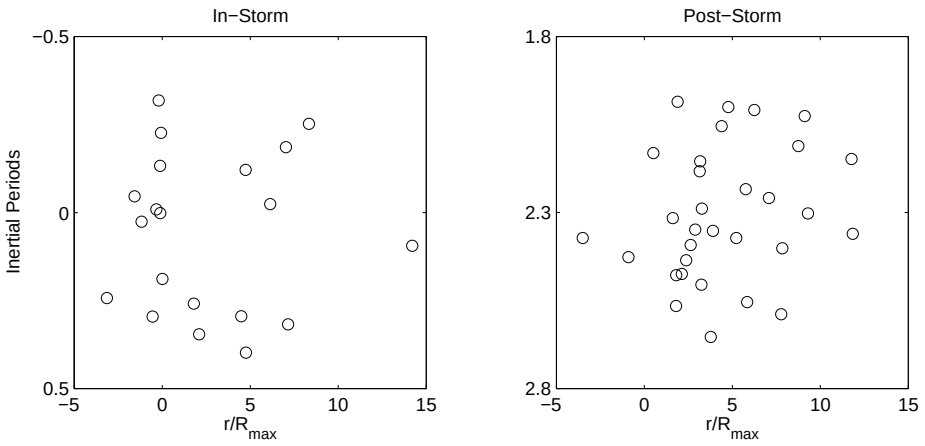

Figure 42: Storm-relative locations of current profiles for in-storm (left) and post-storm (right) analyses. Storm center is at origin, and track is from bottom to top of plots along 0 r/R_{max}. Roughly 3/4 wavelength of the near-inertial wake is sampled.

Next the forced near-inertial currents are estimated from observed residual currents $\vec{u}-\vec{u}_g$. The residual current profiles are fit to the near-inertial model of Rossby and Sanford (1976), as demonstrated by Shay et al. (1998):

$$u_i = [C_u \cos(\sigma t) + S_u \sin(\sigma t)]e^{-t/4\mathrm{IP}} + u_r, \quad (51)$$

$$v_i = [C_v \cos(\sigma t) + S_v \sin(\sigma t)]e^{-t/4\mathrm{IP}} + v_r. \quad (52)$$

As was done for the orbital velocity fitting, the profiles are fit to the model using the Levenberg-Marquardt technique. Estimating the near-inertial current response from the observed current profiles is left as a future research task.

c. Budget terms

1) MECHANICAL ENERGY

Equation 35 expressed the mean OML KE balance, and forms the basis for evaluating the budget of mechanical energy. The relevant quantities (near-inertial and geostrophic currents, OML depth and mass distribution, and thermocline stratification) will be estimated and the KE advection, PE and pressure work terms computed. Hurricane Lili traversed a region observed to have three distinct structures: 1) the deep, warm core of the LC system with low stratification and weak background geostrophic flow; 2) the LC itself with strong geostrophic currents, varying OML depth and stratification; and 3) the GCW with weak background flow, shallow OML depth and stronger stratification. It is clear that certain processes will be dominant depending upon the location within the observed domain, and it is proposed to estimate budget quantities separately for each location.

Because the Coriolis acceleration acts normal to the direction of the horizontal current, the effect of planetary rotation does not appear in the energy balance. Being so, the balanced geostrophic current represents a state of zero energy conversion. Considering a simplified form of the mechanical energy equation by neglecting advection and surface fluxes:

$$\frac{\partial}{\partial t}\left[\frac{\vec{u}\cdot\vec{u}}{2}+gz\right]=f\mathbf{k}\cdot(\vec{u}\times\vec{u}_g), \tag{53}$$

it is clear that when the flow is purely geostrophic, the mechanical energy is conserved. Correspondingly, it is the *departure* from geostrophy (i.e. the storm-forced inertial current) which contributes to the energy balance through the pressure gradient force. Evaluation of the surface fluxes of energy, since they will depend highly upon the choice of parameterization, is a separate research objective.

2) VORTICITY

The vorticity budget terms in Equation 37 (stretching, advection) for both geostrophic and near-inertial currents may now be estimated from observations. The total horizontal current $\vec{u}$ is considered to be composed of geostrophic and ageostrophic (near-inertial) components. In the absence of advection and external torques, the rate of change of relative vorticity of the total current depends only on the divergence of the near-inertial current:

$$\frac{\partial \zeta}{\partial t} = -f\left(\nabla \cdot \vec{u}_i\right). \tag{54}$$

Therefore, identifying the departure from geostrophy determines the stretching term of the OML vorticity budget. As with energy budget, the surface stress curl terms (top and bottom of the OML) are the subject of a separate research objective in the next section.

6. Surface fluxes

A second objective of this research is to examine relationships between the surface energy and momentum fluxes into the ocean, as computed from the budget analyses, to the KE and momentum losses within a mature TC. The OML energy budget analysis yields an estimate of the net energy flux, and the net surface stress curl is computed from the vorticity budget. These two flux quantities are related to one another by a characteristic velocity scale which is responsible for the coupling. The energy flux is the scalar product of two vectors, opening the possibility of zero or even negative fluxes (i.e. from ocean to atmosphere) if the vectors are orthogonal or directed opposite. At the very least, significant asymmetries in surface fluxes are likely even under "axisymmetric" forcing, due in part to inhomogeneous ocean conditions described above.

a. OML base shear stresses

A primary research objective involves computing surface fluxes at the top of the OML (i.e. the air-sea interface), therefore an estimate of the fluxes at the base of the OML is necessary. Turbulent mixing is predicted to be the dominant physical process across this shear zone, and it is the entrainment of the colder waters from the thermocline into the OML that is responsible for most of the OML cooling induced by TCs (Price 1981). Direct turbulence measurements, that is, high frequency point measurements of current data, were not obtained as part of the research experiments. Thus, a closure method is required to estimate the OML base shear stress in terms of the observed mean variables. With available estimates of the shear stress across the OML base, the fluxes of energy (E_M) and vorticity (V_M) can be computed, leaving the air-sea flux terms (E_W and V_W) as unknowns in the budget equations.

From Garwood (1977), the shear stress vector at the base of the OML can be expressed as:

$$\vec{\tau}_{-h} = \rho_0 \, w_e \, \delta\vec{u}, \tag{55}$$

where $\delta\vec{u}$ represents the velocity perturbation at the base of the OML, and w_e is the entrainment velocity which is equal to the OML thickness rate of change due to net turbulent mixing processes. Jacob and Shay (2003) and Jacob et al. (2000) review several parameterization methods for estimating w_e. The closures are based on assumptions regarding the dominant terms in the turbulent kinetic energy budget, and in general relate w_e to the surface stress, surface heat flux, and the mean current shear at the OML base. Each process has been found to be dominant in different portions of tropical cyclones, so no one universal closure has been identified. Jacob and Shay (2003) found that the parameterization of Pollard et al. (1973), which was also applied in the modeling study of (Price 1981), produced the most accurate overall results in the OML thermal response. Since this scheme is based upon a bulk Richardson number, and therefore observed shear, its accuracy seems reasonable since it is expected that the shear stress at the OML base will be the dominant mixing mechanism.

Entrainment velocity is computed by:

$$w_e = 5 \times 10^{-4} \, \delta u \, \mathrm{Ri_B}^{-4}, \tag{56}$$

where δu is the current speed jump across the OML base, and Ri_B is the bulk Richardson number, defined here as:

$$\mathrm{Ri_B} = \frac{g \, \alpha \, h \, \delta T}{(\delta u)^2}, \tag{57}$$

where g is the gravitational acceleration, α is the thermal expansion coefficient, and δT is the temperature

jump at the OML base. In practice, w_e is set to zero where $\mathrm{Ri_B} > 1$, and as such, mixing ceases. This particular parameterization avoids uncertainty in surface forcing (i.e. u_*), upon which other parameterizations are based (e.g. Kraus and Turner (1967); Denman (1973)). With an estimate of w_e available, $\vec{\tau}$ may be estimated. Finally, the energy and vorticity fluxes at the OML base can be estimated as:

$$E_M = [\vec{u} \cdot \vec{\tau}]_{-h}, \tag{58}$$

$$V_M = \frac{1}{\rho_0}[\mathbf{k} \cdot (\nabla \times \vec{\tau})]_{-h}. \tag{59}$$

For the case of the energy flux at $-h$, $\vec{u}$ and $\vec{\tau}$ are assumed aligned to one another, and the direction of flux is determined only by the sign of τ (positive equals downward flux).

b. Wind stress curl and momentum flux

With the curl of the shear stress at the OML base (V_M) computed, the vorticity equation (Equation 37) is rearranged such that the left-hand side contains all known terms leaving the wind stress curl as the unknown right-hand side:

$$\zeta_t + V_A + V_S + V_M = V_W. \tag{60}$$

To obtain the non-divergent portion of the wind stress $\vec{\tau}$, V_W must be inverted with boundary conditions. First, a potential function is defined in terms of the wind stress vector components analogous to a stream-function:

$$\tau_x = \frac{\partial \psi}{\partial y}, \quad \tau_y = -\frac{\partial \psi}{\partial x}. \tag{61}$$

Cross differentiating and subtracting terms gives the wind stress curl in terms of a Laplacian:

$$\rho_0 \, V_W = \nabla^2 \psi. \tag{62}$$

This particular expression is inverted to obtain $\psi(x, y)$, from which the non-divergent portion of the wind stress vector $\vec{\tau}$ is recovered by differentiation. The surface wind field can be utilized to estimate the total wind stress (i.e. irrotational plus non-divergent components) based upon the radial (divergent) component of the surface wind.

How the momentum transfer is accomplished, and how it relates to a momentum loss in the atmosphere, is now briefly examined. Csanady (2001) discusses the momentum transfer pathways and provides estimates of the relative magnitudes for each possibility. In a turbulent shear flow over the open ocean, momentum transfer is facilitated via both viscous shear stress and pressure forces due to form drag over steep waves. Viscous stress transfers momentum to both long waves and directly to the sea surface shear flow, and the short waves receive momentum through form drag via Reynolds stresses. The momentum received by waves is then transfered to the OML upon breaking (Craig and Banner 1994). It is estimated that roughly comparable percentages of momentum are transfered from the atmosphere to OML via the short wave breakers and direct viscous stress, with a much smaller amount through long waves (Csanady 2001).

Following Lionello et al. (1996), the net downward momentum flux from the atmosphere is:

$$\tau_a = \tau_{aw} + \tau_{ao}, \tag{63}$$

where the subscripts a, w, and o denote the atmosphere, wave, and ocean, respectively. The "wave-induced" stress, τ_{aw}, represents the momentum transfer from wind to short waves, and τ_{ao} is the direct

momentum flux from the atmosphere to the ocean via viscous stress. The momentum flux into the ocean, estimated in the budget analysis as part of this research, is:

$$\tau_o = \tau_{ao} + \tau_{wo}. \tag{64}$$

The net momentum flux to the waves is thus $\tau_w = \tau_{aw} - \tau_{wo}$. In an equilibrium sea of infinite fetch and duration, $\tau_w = 0$ and $\tau_a = \tau_o$. The ratio τ_{aw}/τ_a is governed by the wave development, and may vary from 0.15-1.0, which is consistent with the discussion in Csanady (2001). On the other hand, most of the momentum transferred to the waves from the wind eventually ends up in the OML upon breaking (97%, Richman and Garrett (1977)).

An example of the estimated momentum flux from the atmosphere (τ_a) is now described. The surface wind field shown in Figure 2 is combined with a particular drag coefficient formulation, giving the surface stress. For this particular example, the Garratt (1977) drag coefficient formulation is chosen with the drag coefficient capped at 2.5×10^{-3}, which corresponds to a wind speed of around 26 $\mathrm{m\,s^{-1}}$. Additionally, since the OML relative vorticity budget is analyzed, the wind stress curl is computed. Figure 43 shows the momentum flux and the wind stress curl fields. The maximum stress magnitude is estimated to be around 6.6 $\mathrm{N\,m^{-2}}$, and the maximum stress curl is around 6.9×10^{-4} $\mathrm{N\,m^{-3}}$. Except for a small region of intense cyclonic vorticity concentrated in the storm's inner core, stress curl is negative over most of the observation domain, due to shear vorticity dominance over curvature vorticity.

The momentum flux on the atmospheric side of the interface is sensitive to the drag coefficient, and any estimate should be accepted with caution in the TC wind speed range. It is the goal of this work to attempt to reconcile τ estimates on both sides of the interface over the scale of TC forcing.

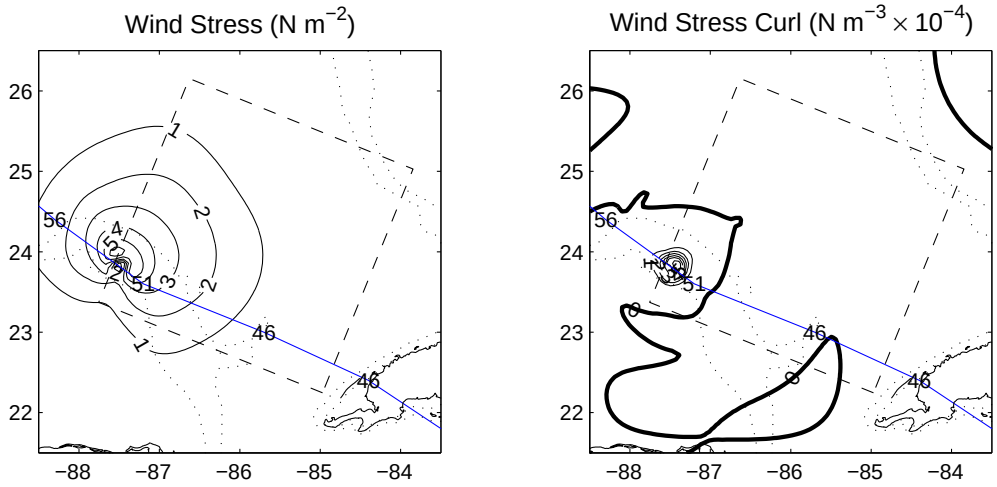

Figure 43: Wind stress magnitude (left panel) and wind stress curl (right panel) computed from the analyzed surface wind field with the drag coefficient formulation of Garratt (1977). The wind stress maximum magnitude is estimated to be 6.6 $\mathrm{N\ m^{-2}}$, The wind stress curl maximum value is approximately 6.9×10^{-4} $\mathrm{N\ m^{-3}}$, though much of the ocean surface, especially on the right side of the storm, experiences a slight anti-cyclonic torque (i.e. negative wind stress curl).

c. Energy fluxes

1) OCEAN SIDE

The energy flux at the air-sea interface is:

$$E_W = k_t + E_A + E_B - E_P - E_M \tag{65}$$

$$= [\vec{u} \cdot \vec{\tau}]_{-h}. \tag{66}$$

Implicit in this expression is knowledge of the velocity $\vec{u}$ through which the energy flux is coupled to the wind stress. In the simple scaling analysis noted above, this velocity was assumed to scale with OML current speed U.

Following Lionello et al. (1996), the energy flux from the atmosphere consists of two components, one

route to the waves, and the other directly to the ocean:

$$\phi_a = \phi_{aw} + \phi_{ao}. \tag{67}$$

The energy flux from wind to waves is related to the momentum flux by:

$$\phi_{aw} \simeq \overline{c}\tau_{aw}, \tag{68}$$

where $\overline{c}$ is the "effective" phase speed of the surface wave responsible for the flux. The energy flux directly to the OML is:

$$\phi_{ao} \simeq u_* \tau_{ao}, \tag{69}$$

with friction velocity u_*. If it is assumed, as before, that comparable amounts of momentum are transfered to waves and directly to the ocean ($\tau_{aw} \simeq \tau_{ao}$), then

$$\frac{\phi_{aw}}{\phi_{ao}} \simeq \frac{\overline{c}}{u_*}. \tag{70}$$

In experimental work, the energy flux is scaled in terms of the observed wave age, c_p/u_*, where c_p is the phase speed at the peak of the wind-sea spectrum. Observations indicate that over the range of wave ages from 4 to 10 (i.e. young seas), $\overline{c} \simeq 0.5c_p$, and decreases to around $0.1c_p$ at $c_p/u_* \simeq 20$ (Terray et al. 1996). For the observed values, an estimate of the ratio of wave to direct ocean energy flux is $\phi_{aw}/\phi_{ao} \simeq 2-5$ for young seas (such as in TCs) and increases to ~ 10 as the sea state matures. As is the case for momentum, it is assumed that most wave energy is eventually lost to the OML upon breaking, and so after some amount of time $\phi_{aw} \simeq \phi_{wo}$. With respect to previous studies, this assumption appears reasonable. Richman and Garrett (1977) indicate that only around 4-9% of the total atmospheric energy transfer will terminate in

the surface wave field. The variability of this value depends upon the development of the wind sea (i.e. fetch), with an increase in the percentage with decreased fetch. Lionello et al. (1998) suggest a slightly larger amount, $\sim 15\%$.

2) ATMOSPHERE SIDE

The KE loss from the atmospheric surface layer is now examined by considering the energy budget on the atmospheric side of the interface. Assuming steady, neutrally stratified, horizontally homogeneous conditions, Equation 21 reduces to:

$$\frac{\partial(u\tau_a)}{\partial z} + p'\frac{\partial w}{\partial z} = \epsilon, \tag{71}$$

where the wind and stress vectors are aligned so that the magnitudes may be examined, and ϵ is the dissipation rate of KE. The turbulent atmospheric surface layer is typically assumed to be a constant stress layer ($\partial\tau_a/\partial z = 0$), and the surface layer energy balance becomes:

$$\tau_a\frac{\partial u}{\partial z} + p'\frac{\partial w}{\partial z} = \epsilon. \tag{72}$$

In the surface layer under high winds, the shear is very large, and shear production and dissipation are in approximate equilibrium:

$$\tau_a\frac{\partial u}{\partial z} = \epsilon. \tag{73}$$

The wind stress is related to the friction velocity u_* by:

$$\tau_a = \rho_a\, u_*^2, \tag{74}$$

where ρ_a is the atmospheric density at the air-sea interface. Under mixing-length theory, the shear is:

$$\frac{\partial u}{\partial z} = \frac{u_*}{\kappa z}, \tag{75}$$

where κ is the von Karman constant and, upon integration over the surface layer depth, leads to the classic logarithmic wind profile:

$$u(z) = \frac{u_*}{\kappa} \ln\left(\frac{z}{z_0}\right), \tag{76}$$

The roughness length, z_0, represents the virtual origin at which the wind vanishes in a log-layer.

Substitution of Equations 74 and 75 into Equation 73 gives the surface layer energy balance:

$$\frac{\rho_a u_*^3}{\kappa z} = \epsilon. \tag{77}$$

Thus, the power generated (and equivalently dissipated) per unit volume within the atmospheric surface layer is proportional to the cube of the friction velocity. Integrating the energy relation over the depth of the surface layer yields an expression for the average energy dissipation per unit area (Businger and Businger 2001):

$$\frac{\rho_a u_*^3}{\kappa} \ln\left(\frac{z}{z_0}\right) = \overline{\epsilon} z. \tag{78}$$

It has been recognized in a number of studies (Bister and Emanuel 1998; Zhang and Altschuler 1999; Businger and Businger 2001) that under intense surface winds such as in TCs, the KE dissipation into internal energy may represent a significant heat source within the surface layer. This term is generally not included in operational numerical forecast models of TCs. A study by Bister and Emanuel (1998) concluded that including this term in the thermal energy equation increased a cyclone's simulated intensity by 20%.

From the surface (10 m) wind analysis of Hurricane Lili shown in Figure 2, the horizontal distribution of the surface layer KE dissipation can be computed, provided a reasonable parameterization of the surface drag. Figure 44 shows the dissipation rate ($\overline{\epsilon}$) computed from the surface wind field using the Garratt (1977) parameterization for C_d. The maximum estimated KE dissipation rate ($\sim 350 \mathrm{W\,m^{-2}}$) represents a

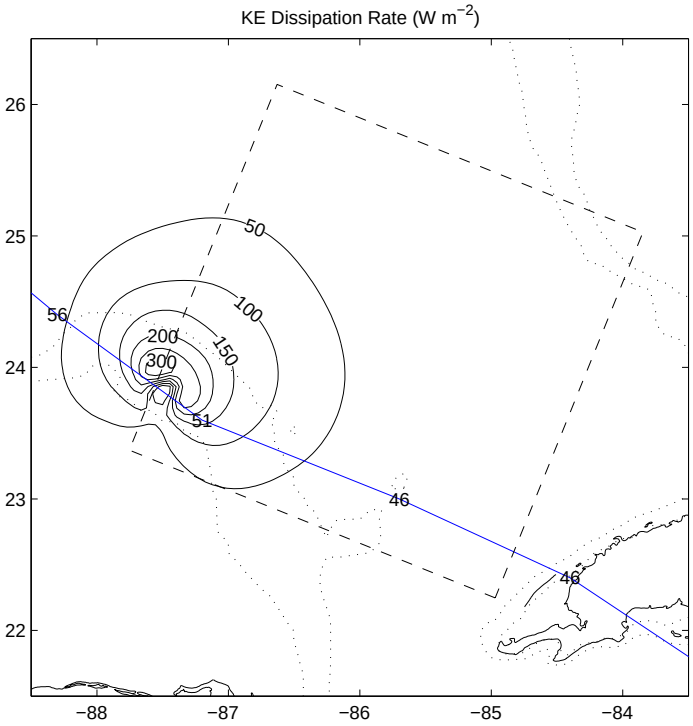

Figure 44: Surface wind KE dissipation rate ($\mathrm{W\,m^{-2}}$) in Hurricane Lili on 2 October 2002. The dissipation rate is computed from the surface wind field combined with the C_d formulation of Garratt (1977). The maximum energy dissipation rate over a surface layer of (arbitrarily chosen) 100 m depth is around 350 $\mathrm{W\,m^{-2}}$.

significant percentage of the maximum enthalpy flux in the high wind inner core of a TC, which has been estimated from ABL budget studies to be on the order of 1200 $\mathrm{W\,m^{-2}}$for storms of similar intensity (e.g. Barnes and Powell (1995)).

Insofar as the assumption that the air-sea interface can be treated analogous to a wall, such that the time evolution scales of the atmospheric shear layer and the growth of surface wind waves are significantly separate, this estimate is reasonable (Donelan 1990). The expression in Equation 78 results from the assumption that the KE lost due to friction is dissipated entirely into heat within the boundary layer.

A recent analysis of hurricane wind profiles from GPS dropwindsondes (Powell et al. 2003) shows that an approximate logarithmic shape holds over a broad range of wind speeds within the ABL. Thus an approximate shear/dissipation balance is confirmed within observational error limits.

From an oceanic standpoint, qualitative observation alone suggests that this is not a complete statement of the energy balance at the sea surface. The statement that all KE generated by shear is dissipated implies that no energy is available for transfer to the ocean ($\phi_a = 0$) even under conditions of constant stress within the ABL. Since there is a growth of surface wave energy under windy conditions, there must be an energy flux out of the ABL to the ocean. It is estimated that this energy flux to the sea surface is only a small percentage of that retained within the ABL (Richman and Garrett 1977; Zhang and Altschuler 1999), so as to justify the approximation of shear/dissipation balance within the atmosphere. Again, it is of primary interest for the research to examine the energy flux to the ocean (ϕ_o) from a TC, and place these estimates within the context of the parameterization-dependent measurement of energy flux from the ABL.

d. Surface heat fluxes

Finally, an estimate of the surface heat (sensible and latent) flux distribution is made. It is of interest to compare observed fluxes of mechanical energy from the atmosphere to ocean with thermodynamic energy flux estimates from the ocean to the atmosphere, since this balance is important for a TC's maintenance. From the surface measurements of temperature, pressure, humidity, and winds shown in Figure 3, the sensible and latent heat fluxes are computed using the Garratt (1977) drag coefficient formulation and arbitrarily assuming the heat and moisture exchange coefficients are equal to C_d. Results are plotted in Figure 45.

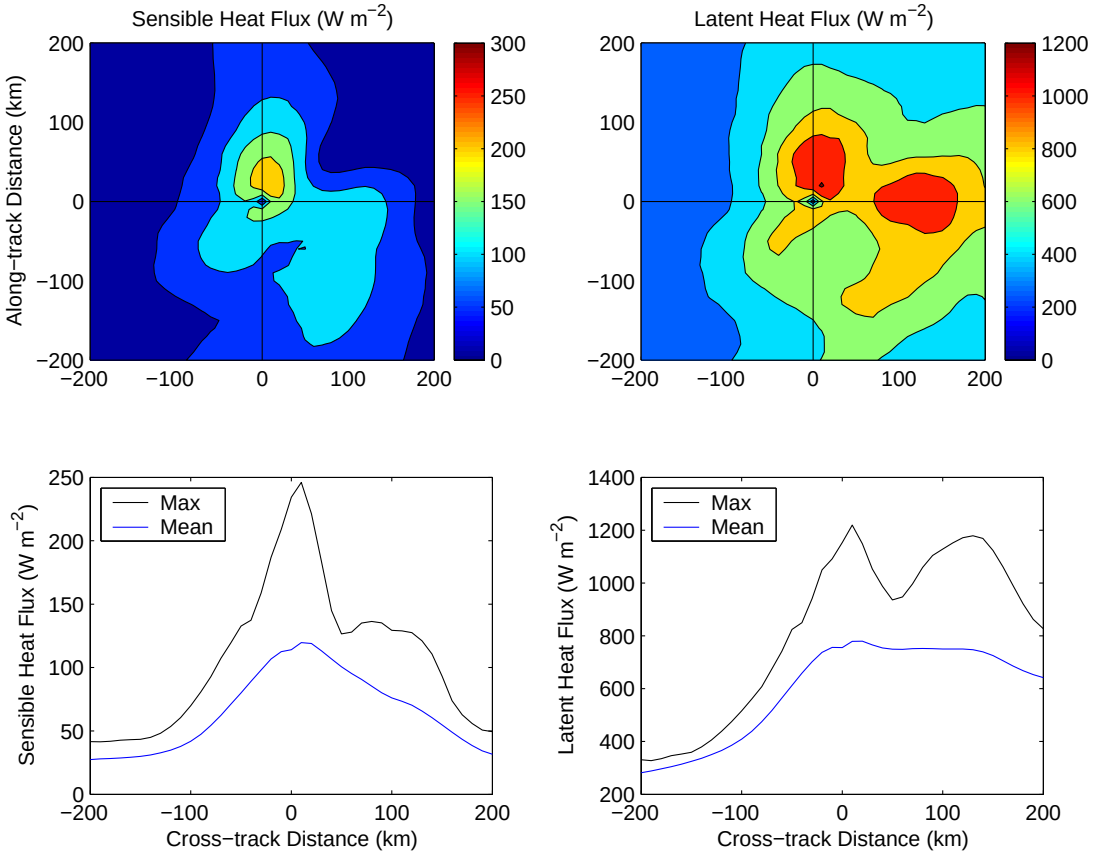

Figure 45: Storm-relative distribution of surface sensible and latent heat fluxes in Hurricane Lili. Top panels show the horizontal fields, and the bottom panels show the along-track maxima and average values.

7. Operational Coupled Model Evaluation

The Geophysical Fluid Dynamics Laboratory (GFDL) (Kurihara et al. 1995) became the official operational hurricane prediction model for the National Weather Service in 1995. Hurricane track forecasts have shown improved accuracy (Kurihara et al. 1998), but the model intensity predictions have shown little skill relative to climatology. A number of reasons for this weakness have been suggested, including initialization procedures, model resolution, and neglecting ocean interaction (Bender et al. 1993). To improve the representation of coupled model physics, the GFDL model has recently been run operationally coupled to a high-resolution version of the Princeton Ocean Model (POM) (Bender and Ginis 2000), and has shown some improvement in intensity prediction. Conclusions about this improvement have usually involved simple comparisons of simulated versus observed minimum central pressure or maximum sustained winds, without any detailed diagnostic analyses of coupled momentum and energy interactions described herein.

GFDL ocean model fields for Hurricane Lili have kindly been provided by I. Ginis (URI) through T. Marchok (NCEP). A plot of surface (5 m depth) currents and temperature from the GFDL coupled model is shown in Figure 46, for the initial model field at 00 UTC on 03 Oct. 2002. The salient features are the extensive wake of strong surface currents and significant cooling, and a remnant Loop Current which appears to have been significantly altered due to passage of the storm. Figure 47 shows the initial model surface stress field for the 02 Oct. 06 UTC run, which may be compared with the observed surface stress shown previously in Figure 43. The maximum surface stress is $\sim$5.7 $\mathrm{N\,m^{-2}}$, which compares reasonably well with that observed ($\sim$6.6 $\mathrm{N\,m^{-2}}$). On the other hand, the vortex center is displaced roughly 80 km to the right of its actual observed location.

Model fields of OML currents indicate maximum storm generated current speeds generated by the storm of around 2.5 $\mathrm{m\,s^{-1}}$, which is commensurate with intense current shears and strong surface cooling,

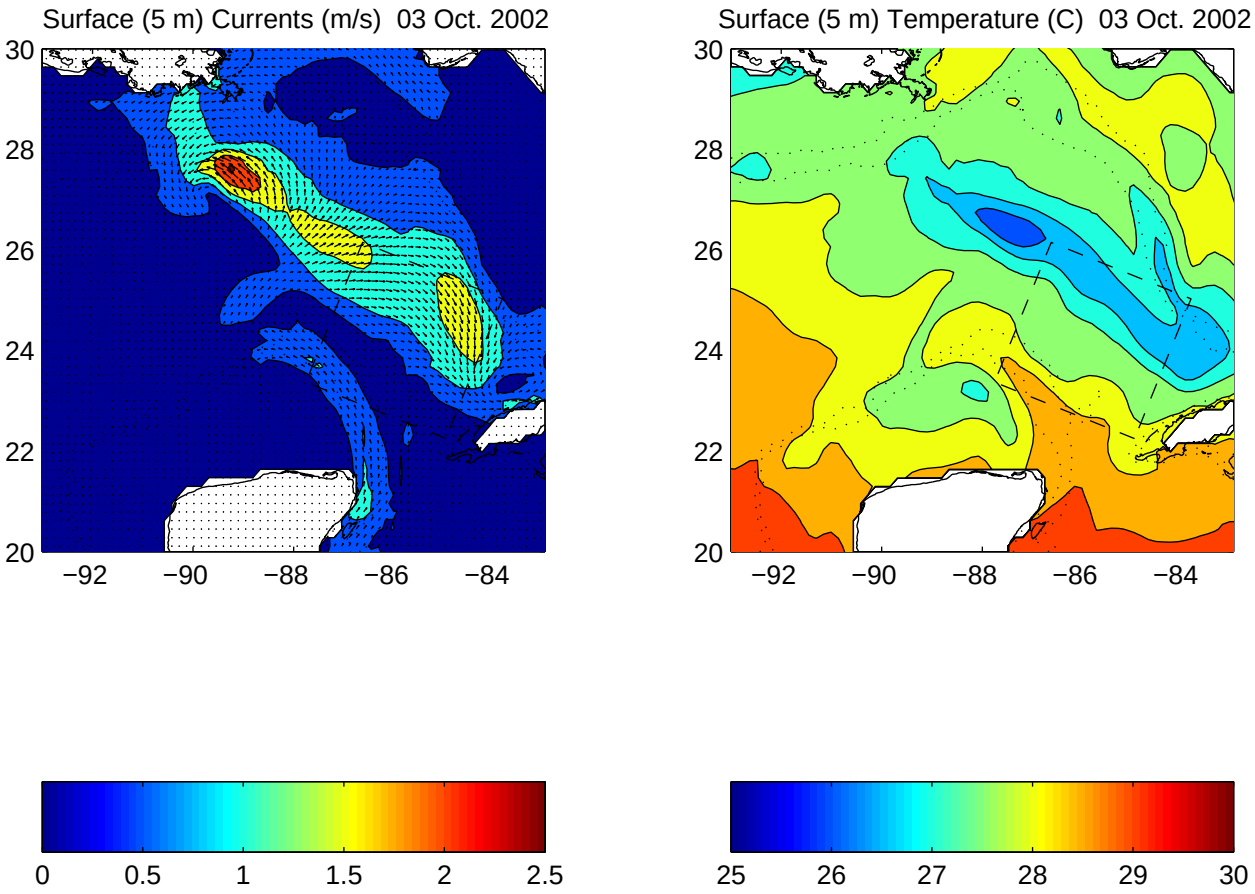

Figure 46: GFDL model initial surface current and temperature field for 00 UTC run on 03 Oct. The dashed box delineates the observational analysis region.

especially in the Loop Current region. This simulated current response is about twice that observed, or around four times the observed KE gain. Additionally, the simulated surface current is around five times greater than scaled wind-drift current estimates indicate. Paradoxically, the operational coupled runs of the GFDL model for Lili showed a consistent bias toward over-intensification relative to that observed (S. Aberson – personal communication). This prompts the following question: How can the model predict the large over-acceleration of the upper-ocean current, presumably at the expense of the storm, while simultaneously maintaining or intensifying the vortex?

To attempt to answer this question, budget analyses are proposed of upper-ocean quantities in the GFDL coupled model similar to that for the observational data. Analyses will focus primarily on relating

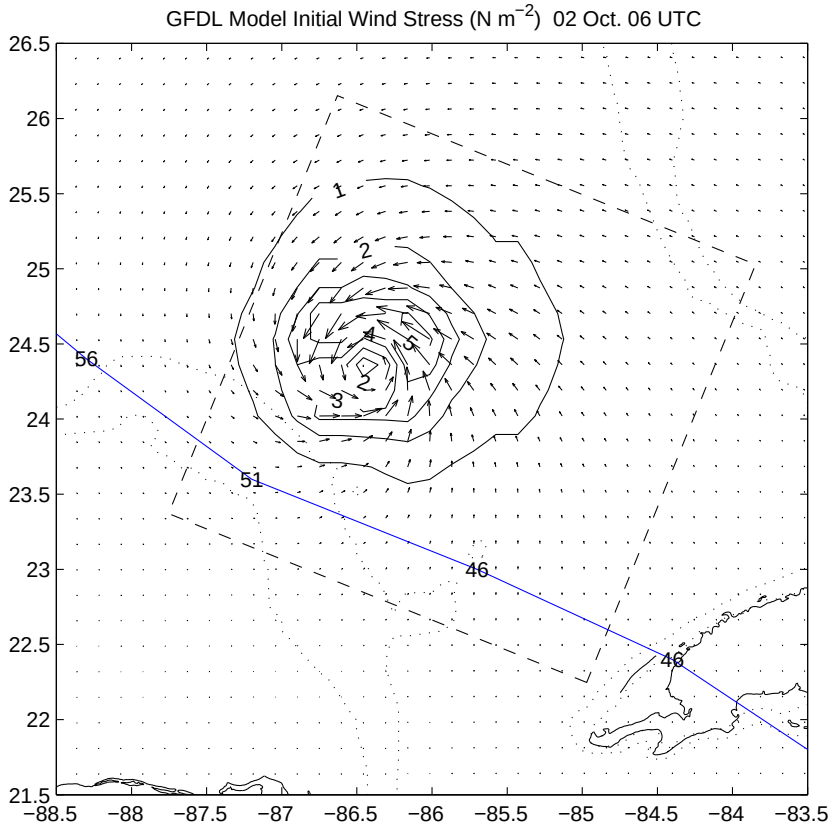

Figure 47: GFDL model initial wind stress field for 06 UTC run on 02 Oct. Maximum stress is around 5.7 $\mathrm{N\ m^{-2}}$, and storm center is mislocated around 80 km to the NE of the observed 06 UTC position, indicated by the "51" along the track.

OML kinetic energy and vorticity changes to surface fluxes implied in the model stress fields.

8. Timeline

The following table details the steps necessary to complete the proposed research along with expected completion dates for each task:

Task	****Completion***
Analysis of OML currents • Estimation of inertial currents • Calculation of shear stresses • Estimation of energy flux and wind stress curl at OML base	July 2005
Error analysis • Observational errors • Budget quantity errors • Mapping errors	September 2005
Surface flux estimation • Calculations from budget analyses • Estimation from wind field	November 2005
Manuscript (Pt. I/II) submission	Fall 2005
Coupled model evaluation • Budget calculations • Comparisons with observational results	Spring 2006
Manuscript (Pt. III) submission	Spring 2006
Dissertation defense	May 2006

*Task completion dates are contigent upon obligations to NOAA Hurricane Field Program during 2005 season.

References

Alamaro, M., K. Emanuel, J. Colton, W. McGillis, and J. Edson, 2002: Experimental investigation of air-sea transfer of momentum and enthalpy at high wind speed. *Preprints, 25th. Conf. on Hurricanes and Tropical Meteorology*, Amer. Meteor. Soc., San Diego, CA, 667–668.

Andreas, E. L. and K. A. Emanuel, 2001: Effects of sea-spray on tropical cyclone intensity. *J. Atmos. Sci.*, **58**, 3741–3751.

Barnes, G. M. and M. D. Powell, 1995: Evolution of the inflow layer of Hurricane Gilbert. *Mon. Wea. Rev.*, **123**, 2348–2368.

Bender, M. A. and I. Ginis, 2000: Real-case simulations of hurricane-ocean interaction using a high-resolution coupled model: Effects on hurricane intensity. *Mon. Wea. Rev.*, **128**, 917–946.

Bender, M. A., R. J. Ross, R. E. Tuleya, and Y. Kurihara, 1993: Improvements in tropical cyclone track and intensity forecasts using the GFDL initialization system. *Mon. Wea. Rev.*, **121**, 2046–2061.

Betts, A. K. and J. Simpson, 1987: Thermodynamic budget diagrams for the hurricane subcloud layer. *J. Atmos. Sci.*, **44**, 842–849.

Bister, M. and K. A. Emanuel, 1998: Dissipative heating and hurricane intensity. *Meteor. Atmos. Phys.*, **65**, 233–240.

Black, P. G., 1983: *Ocean temperature change induced by tropical cyclones*. Ph.D. thesis, The Pennsylvania State University.

Braun, S. A. and W. K. Tao, 2000: Sensitivity of high-resolution simulations of Hurricane Bob (1991) to planetary boundary layer parameterizations. *Mon. Wea. Rev.*, **128**, 3941–3961.

Bretherton, F. P., R. E. Davis, and C. B. Fandry, 1976: A technique for objective analysis and design of experiments applied to MODE-73. *Deep-Sea Res.*, **23**, 559–582.

Brooks, D. A., 1983: The wake of Hurricane Allen in the western Gulf of Mexico. *J. Phys. Oceanogr.*, **13**, 117–129.

Businger, S. and J. A. Businger, 2001: Viscous dissipation of turbulence kinetic energy in storms. *J. Atmos. Sci.*, **58**, 3793–3796.

Chang, S. W. and R. A. Anthes, 1978: Numerical simulations of the ocean's nonlinear baroclinic response to translating hurricanes. *J. Phys. Oceanogr.*, **8**, 468–480.

Craig, P. D. and M. L. Banner, 1994: Modeling wave-enhanced turbulence in the ocean surface layer. *J. Phys. Oceanogr.*, **24**, 2546–2559.

Csanady, G. T., 2001: Drag generation mechanisms. *Wind stress over the ocean*, I. S. F. Jones and Y. Toba, eds., Cambridge University Press, 124–141.

DeMaria, M. and J. Kaplan, 1993: Sea surface temperature and the maximum intensity of Atlantic tropical cyclones. *J. Climate*, **7**, 1324–1334.

Denman, K. L., 1973: A time-dependent model of the upper ocean. *J. Phys. Oceanogr.*, **3**, 173–184.

Donelan, M., 1990: Air-sea interaction. *The Sea: Ocean Engineering Science*, John Wiley & Sons, Inc., volume 9, 239–292.

Donelan, M. A., F. W. Dobson, S. D. Smith, and R. J. Anderson, 1993: On the dependence of sea surface roughness on wave development. *J. Phys. Oceanogr.*, **23**, 2143–2149.

Donelan, M. A., W. M. Drennan, and K. B. Katsaros, 1997: The air-sea momentum flux in conditions of wind sea and swell. *J. Phys. Oceanogr.*, **27**, 2087–2099.

Donelan, M. A., B. K. Haus, N. Reul, M. Stiassne, H. C. Graber, O. B. Brown, and E. S. Saltzman, 2004: On the limiting aerodynamic roughness of the ocean in very strong winds. *Geophys. Res. Lett.*, submitted.

Drennan, W., H. C. Graber, and M. Donelan, 1999: Evidence for the effects of swell and unsteady winds on marine wind stress. *J. Phys. Oceangr.*, **29**, 1853–1864.

Elliot, B. A., 1982: Anticyclonic rings in the Gulf of Mexico. *J. Phys. Oceangr.*, **12**, 1292–1309.

Emanuel, K., 2003: A similarity hypothesis for air-sea exchange at extreme wind speeds. *J. Atmos. Sci.*, **60**, 1420–1428.

Emanuel, K. A., 1986: An air-sea interaction theory for tropical cyclones. Part I: Steady-state maintenance. *J. Atmos. Sci.*, **43**, 585–604.

— 1995: Sensitivity of tropical cyclones to surface exchange coefficients and a revised steady-state model incorporating eye dynamics. *J. Atmos. Sci.*, **52**, 3969–3976.

Fairall, C. W., J. D. Kepert, and G. J. Holland, 1994: The effect of sea spray on surface energy transports over the ocean. *Global Atmos. Ocean Syst.*, **2**, 121–142.

Fofonoff, P. and R. C. J. Millard: 1983, Algorithms for computation of fundamental properties of seawater. Technical Report 44, UNESCO.

Garratt, J. R., 1977: Review of drag coefficients over oceans and continents. *Mon. Wea. Rev.*, **105**, 915–929.

Garwood, R. W., 1977: An oceanic mixed layer model capable of simulating cyclic states. *J. Phys. Oceanogr.*, **7**, 455–468.

Geisler, J. E., 1970: Linear theory on the response of a two-layer ocean to a moving tropical cyclone. *Geophys. Fluid. Dyn.*, **1**, 249–272.

Hanson, J. L. and O. M. Phillips, 1999: Wind sea growth and dissipation in the open ocean. *J. Phys. Oceanogr.*, **29**, 1633–1648.

Hock, T. F. and J. L. Franklin, 1999: The NCAR GPS dropwinsonde. *Bull. Amer. Meteor. Soc.*, **80**, 407–420.

Huang, N. E., 1986: An estimate of the influence of breaking waves on the dynamics of the upper ocean. *Wave Dynamics and Radio Probing of the Ocean Surface*, O. M. Phillips and K. Hasselmann, eds., Plenum Press, volume 1, 295–318.

Jacob, S. D. and L. K. Shay, 2003: The role of ocean mesoscale features on the tropical cyclone-induced mixed layer response: A case study. *J. Phys. Oceanogr.*, **33**, 649–676.

Jacob, S. D., L. K. Shay, A. J. Mariano, and P. G. Black, 2000: The 3-D oceanic mixed layer response to Hurricane Gilbert. *J. Phys. Oceanogr.*, **30**, 1407–1429.

Kara, A. B., P. A. Rochford, and H. E. Hurlburt, 2000: An optimal definition for ocean mixed layer depth. *J. Geophys. Res.*, **105**, 16803–16821.

Katsaros, K. B., S. D. Smith, and W. A. Oost, 1987: HEXOS–Humidity Exchange over the Sea, a program for research on water-vapor and droplet fluxes from sea to air at moderate to high wind speeds. *Bull. Amer. Meteor. Soc.*, **68**, 466–476.

Kraus, E. B. and J. S. Turner, 1967: A one-dimensional model of the seasonal thermocline. II: The general theory and its consquences. *Tellus*, **19**, 98–106.

Kundu, P. K.: 1990, *Fluid mechanics*, Academic Press, chapter 15. 638.

Kurihara, Y., M. A. Bender, R. E. Tuleya, and R. J. Ross, 1995: Improvements in the GFDL hurricane prediction system. *Mon. Wea. Rev.*, **123**, 2791–2801.

Kurihara, Y., R. E. Tuleya, and M. A. Bender, 1998: The GFDL hurricane prediction system and its performance in the 1995 hurricane season. *Mon. Wea. Rev.*, **126**, 1306–1322.

Large, W. G. and S. Pond, 1981: Open ocean momentum flux measurements in moderate to strong winds. *J. Phys. Oceanogr.*, 324–336.

Leipper, D. F., 1967: Observed ocean conditions in Hurricane Hilda. *J. Atmos. Sci.*, **24**, 182–196.

Lionello, P., K. Hasselmann, and G. L. Mellor, 1996: On the coupling between a surface wave model and a model of the mixed layer of the ocean. *The air-sea interface: Radio and acoustic sensing, turbulence, and wave dynamics*, M. A. Donelan, W. H. Hui, and W. J. Plant, eds., The Rosenstiel School of Marine and Atmospheric Science, University of Miami, 195–201.

Lionello, P., P. Malguzzi, and A. Buzzi, 1998: Coupling between the atmospheric circulation and the ocean wave field: An idealized case. *J. Phys. Oceanogr.*, **28**, 161–177.

Malkus, J. S. and H. Riehl, 1960: On the dynamics and energy transformations in steady-state hurricanes. *Tellus*, **12**, 1–20.

Mariano, A. J. and O. B. Brown, 1992: Efficient objective analysis of heterogeneous and non-stationary fields via parameter matrix. *Deep-Sea Res. Part A.*, **23**, 1255–1271.

Marquardt, D., 1963: An algorithm for least squares estimation of non-linear parameters. *J. Soc. Ind. Appl. Math.*, **11**, 431–441.

Millero, F. J., C. T. Chen, A. Bradshaw, and K. Schleicher, 1980: A new high pressure equation of state for seawater. *Deep Sea Res.*, **27A**, 255–264.

O'Brien, J. J. and R. O. Reid, 1967: The non-linear response of a two-layer, baroclinic ocean to a stationary, axially-symmetric hurricane: Part I: Upwelling induced by momentum transfer. *J. Phys. Oceanogr.*, **24**, 197–207.

Ooyama, K., 1969: Numerical simulation of the life cycle of tropical cyclones. *J. Atmos. Sci.*, **26**, 3–40.

Palmen, E., 1948: On the formation and structure of tropical cyclones. *Geophysica*, **3**, 26–38.

Pollard, R. T., P. B. Rhines, and R. O. R. Y. Thompson, 1973: The deepening of the wind driven layer. *Geophys. Fluid Dyn.*, **4**, 381–404.

Powell, M., P. J. Vickery, and T. A. Reinhold, 2003: Reduced drag coefficient for high wind speeds in tropical cyclones. *Nature*, **422**, 279–283.

Powell, M. D., S. H. Houston, L. R. Amat, and N. Morisseau-Leroy, 1998: The HRD real-time hurricane wind analysis system. *J. Wind Engr. Ind. Aerody.*, **77-78**, 53–64.

Price, J. F., 1981: Upper ocean response to a hurricane. *J. Phys. Oceanogr.*, **11**, 153–175.

— 1983: Internal wave wake of a moving storm. Part I: scales, energy budget and observations. *J. Phys. Oceanogr.*, **13**, 949–965.

Richman, J. and C. Garrett, 1977: The transfer of energy and momentum by the wind to the surface mixed layer. *J. Phys. Oceanogr.*, **7**, 876–881.

Rosenthal, S. L., 1971: The response of a tropical cyclone model to variations in boundary layer parameters, initial conditions, lateral boundary conditions and domain size. *Mon. Wea. Rev.*, **99**, 767–777.

Rossby, H. T. and T. B. Sanford, 1976: A study of velocity profiles through the main thermocline. *J. Phys. Oceanogr.*, **6**, 766–774.

Sanford, T. B., P. G. Black, J. Haustein, J. W. Fenney, G. Z. Forristall, and J. F. Price, 1987: Ocean response to hurricanes. Part II: Observations. *J. Phys. Oceanogr.*, **17**, 2065–2083.

Sanford, T. B., R. G. Drever, J. H. Dunlap, and E. A. D'Asaro: 1982, Design, operation, and performance of an expendable temperature and velocity profiler (XTPV). Technical report, Applied Physics Lab., University of Washington.

Shay, L. K., P. G. Black, A. J. Mariano, J. D. Hawkins, and R. L. Elsberry, 1992: Upper ocean response to Hurricane Gilbert. *J. Geophys. Res.*, **97**, 20277–20248.

Shay, L. K., S. W. Chang, and R. L. Elsberry, 1990: Free surface effects on the near-inertial ocean current response to a hurricane. *J. Phys. Oceangr.*, **20**, 1405–1424.

Shay, L. K. and R. L. Elsberry, 1987: Near-inertial ocean current response to Hurricane Frederic. *J. Phys. Oceanogr.*, **17**, 1249–1269.

Shay, L. K., R. L. Elsberry, and P. G. Black, 1989: Vertical structure of the ocean current response to a hurricane. *J. Phys. Oceanogr.*, **19**, 649–669.

Shay, L. K., G. J. Goni, and P. G. Black, 2000: Effects of a warm oceanic feature on Hurricane Opal. *Mon. Wea. Rev.*, **128**, 1366–1383.

Shay, L. K. and S. D. Jacob, 2005: Relationship between oceanic energy fluxes and surface winds during tropical cyclone passage. *J. Phys. Oceanogr.*, **6**, In press.

Shay, L. K., A. J. Mariano, S. D. Jacob, and E. H. Ryan, 1998: Mean and near-inertial ocean current response to Hurricane Gilbert. *J. Phys. Oceanogr.*, **28**, 858–889.

Terray, E. M., M. A. Donelan, Y. C. Agrawal, W. M. Drennan, K. K. Kahma, A. J. Williams III, P. A. Hwang, and S. A. Kitaigorodskii, 1996: Estimates of kinetic energy dissipation under breaking waves. *J. Phys. Oceanogr.*, **26**, 792–807.

Uhlhorn, E. W. and P. G. Black, 2003: Verification of remotely sensed sea surface winds in hurricanes. *J. Atmos. Ocean. Tech.*, **20**, 99–116.

Wright, C. W., E. J. Walsh, D. Vandermark, W. B. Krabill, A. W. Garcia, S. H. Houston, M. D. Powell, P. G. Black, and F. D. Marks, 2001: Hurricane directional wave spectrum spatial variation in the open ocean. *J. Phys. Oceanogr.*, **31**, 2472–2488.

Zhang, D.-L. and E. Altschuler, 1999: The effects of dissipative heating on hurricane intensity. *Mon. Wea. Rev.*, **127**, 3032–3038.